2019-04-24

In situ free phase gas production in initially saturated sediment

Abboud, Jason M.

UNIVERSITY OF CALGARY

In situ free phase gas production in initially saturated sediment

by

Jason M. Abboud

A THESIS

SUBMITTED TO THE FACULTY OF GRADUATE STUDIES

IN PARTIAL FULFILMENT OF THE REQUIREMENTS FOR THE

DEGREE OF MASTER OF SCIENCE

GRADUATE PROGRAM IN GEOLOGY AND GEOPHYSICS

CALGARY, ALBERTA

APRIL, 2019

Abstract

Free-phase gas (FPG) formation and migration in gas-saturated groundwater has geological and engineering implications. FPG has been implicated in geologic overpressurizing, and in remote earthquake triggering following FPG exsolution. FPG exsolution occurs when total dissolved gas pressure (P_{TDG}) exceeds porewater pressure (P_W) and capillary pressure (P_{CAP}), forming FPG bodies. Existing soil-water characteristic curves show the relationship between desaturation and matric potential, but neglect desaturation that occurs as a consequence of *in situ* FPG formation. This research sought to observe and characterize FPG production in a previously saturated zone, and measure the responses of P_{TGD}, P_W, and water content during step-function unloading of dissolved gas-charged sediment in a loading cell filled with glass beads. A revised FPG characteristic curve showing FPG formation and consumption with respect to capillary pressure is proposed here. Future work can examine these processes with revised techniques to ensure accurate measurement of capillary pressure.

Acknowledgements

There are several people I would like to thank for their help and support throughout this degree. First off, I'd like to thank my supervisor, Cathy Ryan, for her mentorship and guidance since we started working together in 2014. I am appreciative of Cathy's your trust and encouragement to pursue so many other transformative processes in grad school, and for her tireless support of being my referee for so many opportunities.

I would like to thank Jocelyn Hayley for letting me use her lab space. Jocelyn's trust and support throughout this project have been invaluable. I learned so much from our meetings and she even inspired to dip my toes in geotechnical engineering as a career. Rachel Lauer, graduate school has been so much more fun because our interactions and your mentorship. It was always such a pleasure to stop by her office to talk about whatever was on our minds. Thank you, too, for introducing me to MATLAB. Thanks to Ron Wong for joining my committee despite having many other commitments. His insight has made me a more critical scientist.

This work would have looked a lot different if it was not for Jim Smith. A large part of Jim's, Calgary trip was spent meeting with me and shedding so much light on pressures and bubble physics.

Mirsad Berbic helped an indispensable amount in helping me build the apparatus for this project. Thanks to Farzin Malekani for being a great support and someone to chat with throughout the years

Where would I be without my friends. ES 272 crew, past and present (Randal, Bethany, Jess, Landon, Dylan, Mike, Neil, Yixuan), we've all been there for each other in the peaks and valleys of our grad degrees and look forward to the continued support. I want to thank my other office, ES 107 (Bad Melons et al.) for always taking me in and getting into squash with me. Jaclyn Carter, Graduate College Co-Chair extraordinaire, thank you/sorry!

Last and certainly not least, my family. They have supported me throughout my entire education in so many ways that I can only *try* to reciprocate over my coming career.

Thank you!

Table of Contents

List of Tables

List of Figures and Illustrations

List of Symbols, Abbreviations and Nomenclature

Hydrogeology term [Geotechnical term]	Symbol (Units)	Definition
Atmospheric pressure	P_{ATM} (kPa)	Pressure exerted by the atmospheric column
Bubble [Occluded gas bubble]		Spherical body of free phase gas
Bubbling point/ pressure [liquid/gas saturation ($U_{l/g}$)]	P_{BUB} (kPa)	Point at which gas exsolves from dissolved phase to free phase (also referred to as Ebullition point/pressure
Buoyancy Pressure	P_{BUOY} (kPa)	Upward force exerted by a body of air in a liquid
Capillary pressure	P_{CAP} (kPa)	Pressure exerted by the interphase of two immiscible fluids
Desaturation [gasification]		Replacement of porewater with gas
Entry pressure	P_E (kPa)	Pressure at which the water in the largest pore to begins to drain
Equilibrium	P_{EQ} (kPa)	Total dissolved gas pressure and porewater pressure are no longer changing
Exsolution		Un-mixing of gas in water, or the formation of FPG
Free phase gas (FPG)	FPG	Gaseous phase gas that is found in FPG bodies or bubbles, i.e., not dissolved
FPG body		Discrete pockets of FPG that may or may not be spherical
Free phase gas characterization curve	FPG-CC	Revised soil water characteristic curve for FPG formation
FPG expansion		FPG growth through change in pressure and/or diffusion
FPG migration		Upwards FPG movement due to buoyant forces

FPG nucleation		Incipient bubble formation in a solution
Gas-charged porous media [Gassy soil]		Porous media with dissolved gas pressure that is close to bubbling point
Gas partitioning		Mass transfer between aqueous and gaseous phases
Gas saturation		Amount of dissolved gas in a solution
Gas species		A chemical composition of the gas (e.g., CO_2, CH_4)
Henry's Law coefficient	k_H	proportionality constant between partial pressure of gas and amount of gas dissolved in solution at given a temperature
In situ		in original place/location, i.e., not removed from solution
Porewater pressure	P_W (kPa)	Pressure exerted by the water between within matrix
Residual water		Water remaining in the pore space after the loading cell reaching atmospheric pressure
Saturated zone [Phreatic zone]		Area below the water table
Soil water characteristic curve	SWCC	Tool used to describe pressure-saturation relationships of soils
Supersaturation		See "Ebullition or Bubbling point/Bubbling pressure"
Total dissolved gas pressure	P_{TDG} (kPa)	Pressure exerted by gas in solution,
Vadose Zone [Unsaturated zone]		Area below ground surface that is intermittently saturated
Vapour Pressure	P_{VAP} (kPa)	Pressure exerted by vapour on aqueous phase

Introduction

1.1 Occurrence of Groundwater Gases

Gas species commonly identified in groundwater include oxygen, carbon dioxide, methane, nitrogen, and hydrogen sulfide. Groundwater gases can originate from either atmospheric gases or subsurface processes. Subsurface processes include radiogenic decay [*Cook and Bohlke*, 2000], degassing from crustal material [*Heaton*, 1981], degassing from non-aqueous phase liquid pools, or other biogeochemical reactions in the subsurface (Figure 1.1). Gas found in the subsurface are either dissolved in groundwater (i.e., in the aqueous phase), or become free phase gas (FPG) when the amount of dissolved gas exceeds the solubility of that gas in water (supersaturated). When groundwater gases form in the FPG-producing formation, they travel along a continuous path through faults or fractures, and will surface at a consistent location. Dissolved groundwater gases are subject to advection and dispersion from groundwater movement.

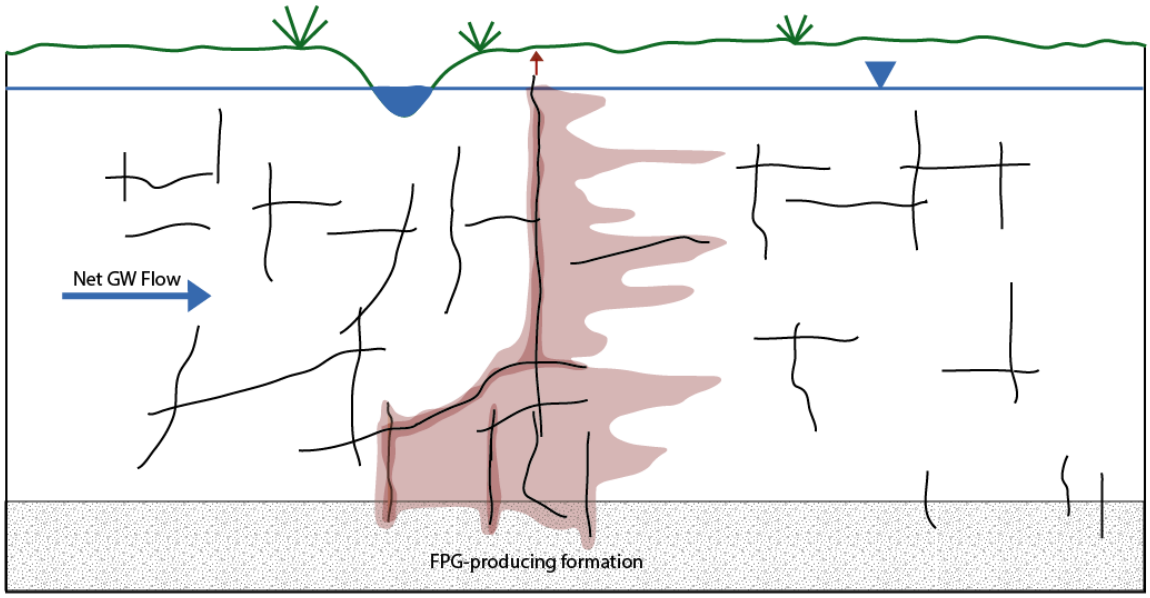

Figure 1.1: Schematic showing FPG originating in the FPG-producing formation, then migrating upwards through cracks and fractures, and being influenced by groundwater flow. FPG reaches ground surface at the same location (adapted from *Ryan* [2017]).

Some common gas-producing groundwater reactions are shown in Table 1.1. Trace gases are also found in the subsurface, and include SF_6, chlorofluorohydrocarbons, and noble gases (such as argon, radon). Notably, radon gas has been the subject of epidemiological and geological studies for its oncogenic properties [*Stanley et al.*, 2017].

Table 2.1: Common groundwater redox reactions involving gaseous compounds (italicized, figure from *Ryan et al.* [2000])

Reaction	Equation
(A) Oxidation of organic carbon	$CH_2O^a + \boldsymbol{O_2} \rightarrow \boldsymbol{CO_2} + H_2O$
(B) Sulfide oxidation[b]	$2\boldsymbol{O_2} + HS^- \rightarrow SO_4^{2-} + H^+$
(C) Denitrification	$4NO_3^- + 5\,CH_2O + 4H^+ \rightarrow 2\boldsymbol{N_2} + 5\,\boldsymbol{CO_2} + 7\,H_2O$
(D) Sulfate reduction	$SO_4^{2-} + 2\,CH_2O \rightarrow \boldsymbol{H_2S} + 2\boldsymbol{CO_2} + 2H^+$
(E) Methane fermentation	$2\,CH_2O + H_2O \rightarrow \boldsymbol{CH_4} + HCO_3^- + H^+$

Field measurements of groundwater gases can be used for tracer experiments [*Wilson and Mackay*, 1996], remediation monitoring [*Amos et al.*, 2005], and groundwater dating [*Aeschbach-Hertig et al.*, 1999], among other processes. Groundwater pumping often results in gas exsolution, or dissolved gas partitioning into free gas, or free phase gas, FPG) which causes reduced flow from gas-locking in the pump tubing [*Alberta Agriculture and Forestry*, 2006], and affects gas sampling from dissolved gas-rich formation. Current investigations are towards developing robust groundwater gas sampling methods [*Ryan et al.*, 2015; *Evans*, 2017].

While this thesis will primarily focus on groundwater gas from a geological and hydrogeological perspective, it is important to note that gas-saturated sediments are also considered in geological and geotechnical engineering investigations. This area of study in engineering is broadly considered as the study of "gassy soils". Unfortunately, there is no unified set of vocabulary that deals with these concepts between geosciences and engineering. The remainder of this thesis primarily uses terminology described in geoscience literature. Please refer to the list of symbols, abbreviations, and nomenclature for synonyms between the fields.

1.2 Geological and Geotechnical Implications of Free Phase Gas

1.2.1 'Dry' Coal Beds

Alberta is home to many coal deposits such as the Paskapoo, Scollard, Belly River, Mannville and Kootenay formations [*Beaton*, 2003], encompassing approximately half of Alberta's geographical area [*Bastian et al.*, 2005]. The Horseshoe Canyon formation, which has been a major coal bed methane play since the early 2000s [*Bastian et al.*, 2005], is 'dry', meaning it does not produce any water [*Bastian et al.*, 2005; *Hoch*, 2005]. The Horseshoe Canyon formation is currently undergoing post-erosional and post-glacial rebound following the Laramide orogeny and Pleistocene glaciation, respectively [*Hoch*, 2005]. The research work performed in this thesis has led to the hypothesis that the Horseshoe Canyon is dry *because of* natural gas production and migration; gas production, indirectly driven by total stress reduction from by glacial rebound, has pushed the water out of this formation over geologic time.

1.2.2 Over-pressurized Units

Certain geological units are over-pressurized meaning that the pore fluids are at a greater pressure than the hydrostatic gradient [*Osborne and Swarbrick*, 1997]. These pressures are significantly greater than the hydrogeologic gradient [*Ingebritsen et al.*, 2011]. Mechanisms leading to over-pressurization are complex, and any combination of tectonic stress, overpressure transfer, and fluid expansion [*Ingebritsen et al.*, 2011] can lead to the reduction in vertical effective stress [*Zhang et al.*, 2016]. Fluid expansion can be directly related to FPG generation and expansion, causing an increase in pore pressure [*Bowers*, 2002; *Ramdhan and Goulty*, 2011]. While over-pressurization can reduce costs of oil and natural gas production, it can also cause tensile fractures and breakouts in wellbores during production [*Fox and Soltanzadeh*, 2015].

1.2.3 Seismicity and Earthquakes

Free phase gas has also been linked to the triggering of remote earthquakes (i.e., a distance away from and following major earthquakes) subsequent to major seismic events [*Crews and Cooper*, 2012]. After initial earthquakes are triggered, seismic waves pass through the subsurface. When these waves pass through aquifers with considerable amounts of dissolved gas, a transient reduction in pore pressure can lead to the bubbling point of dissolved gas in water, and consequently, the exsolution of free phase gas. FPG formation is a rapidly occurring process [*Wong and Maini*, 2007], causing an increase in pore pressure and consequent decrease in effective stress [*Crews and Cooper*, 2014]. This decrease in effective stress then lowers the critical shear stress required to cause fault movement [*Crews and Cooper*, 2014], making remote fault zones more susceptible to earthquake triggering.

Moreover, magmatic gases ($He_{(g)}$ and $CO_{2(g)}$) have also been reported in a remote earthquake triggered after a major event in Japan [*Aizawa et al.*, 2016]. In addition, deep-sourced CO_2 was discovered in a minor earthquake triggered after, and remote from, major events in Italy [*Miller et al.*, 2004].

1.2.4 Deep Marine and Tidal-influenced Environments

Due to the presence of FPG, offshore and marine soils are often not fully saturated, which can impact offshore construction [*Wheeler*, 1988]. The presence of free phase gas can change the volume of the soil in addition to affecting the shear strength [*Amaratunga and Grozic*, 2009], which can cause landslides in submarine settings [*Esrig and Kirby*, 1977]. In addition, tidal drawdown can cause the exsolution of PFG [*Amaratunga and Grozic*, 2009], possibly leading to liquefaction failures [*Haththotuwa and Grozic*, 2011]. These types of failures in offshore sand, and sand/silt-dominated, tidal-affected regions have been reported extensively in British Columbia, the Netherlands, and locations around Scandinavia as early as 1888 [*Haththotuwa and Grozic*, 2011]. In Figure 1.2, the pore pressure response is recorded in a tidal zone [*Christian et al.*, 1997]. The presence of FPG was noted by the lag in response time between the tide and pore pressure response. At low tide, the reduction in total stress lead to the exsolution of FPG, which ultimately reduced the effective stress.

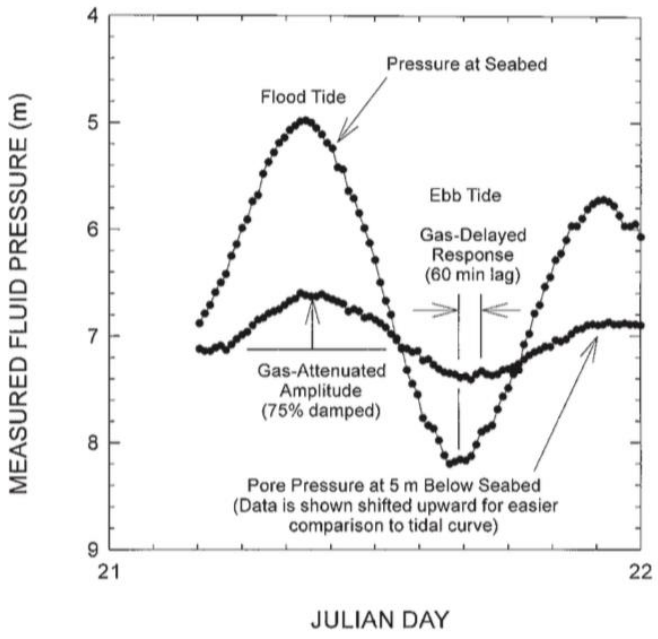

Figure 1.2: Pore pressure response from Fraser River delta seabed. Lag time (60 min) seen between tide level and pore pressure response (From *Christian et al.* [1997]).

Another important natural phenomenon with FPG is in the dissociation of FPG from gas hydrates. Natural gas hydrates are solid clathrates of water with methane trapped inside, and are found at considerable depths and pressures in marine settings (and in continental permafrost regions) [*Ingebritsen et al.*, 2011]. The stability window of methane hydrates is quite narrow, and gas hydrates rapidly dissociate outside of this zone, making the study of gas hydrates technically challenging.

The natural gas reservoir potential of gas hydrates makes these deposits the largest fossil fuel reserve, which has important implications as an energy source, as well as a large contributor to greenhouse gases [*Ingebritsen et al.*, 2011]. Understanding pressure relationships with the dissociation of methane from the water is a critical aspect in understanding how these resources can be exploited.

1.2.5 Oil Sands and FPGs

Free phase gas has also been observed in *in situ* oil sands samples [*Sobkowicz and Morgenstern*, 1984]. Typically, oil sands samples exhibit high compressive strength and low compressibility properties [*Dusseault*, 1979]. When total stress on *in situ* samples is reduced, however, $CO_{2(g)}$ and $CH_{4(g)}$ exsolve in large amounts [*Sobkowicz and Morgenstern*, 1984]. The presence of FPG in these samples affected the compressibility of the soils, reducing effective stress and ultimately reducing the soil strength. Reduced soil strength due to FPG has implications in tailing ponds stability, dyke wall integrity, and reservoir stability in heavy oil mining operations, which could ultimately affect production and reclamation of, and safety in, oil sands operations [*Sobkowicz and Morgenstern*, 1984].

1.3 Governing Equations for Groundwater Gases

1.3.1 Total Dissolved Gas Pressure (P_{TDG}) and Henry's Law

The concept of total dissolved gas pressure measurements was first mentioned by *D'Aoust and Clark*, [1980] and later expanded on by Manning *et al.* [2003] and Roy and Ryan [2010]. Understanding total dissolved gas pressure first requires an understanding of gas solubility and Henry's Law. Henry's Law is used to describe gas solubility for a single gas species gas in water below:

$$C_{aq} = k_H \cdot P \qquad (1.1)$$

where C_{aq} is the dissolved (aqueous) concentration of gas ($mol \cdot L^{-1}$), k_H is the Henry's Law coefficient ($mol \cdot L^{-1} \cdot atm^{-1}$), and P is the pressure of the gas species (kPa).

According to Henry's Law, the concentration of dissolved gas in solution is proportional to the partial pressure of that gas in equilibrium with the aqueous phase, and a constant (called Henry's coefficient) for that gas at a given temperature. As such, at greater partial pressures of gas, there will be a higher concentration of that gaseous species in that solution. Henry's coefficient describes a given gas's propensity to dissolve and remain in solution which is a function of both temperature and salinity of the water, with temperature having a greater effect on the coefficient.

Should more than one gas be present in solution, then a general form of Henry's Law can be used to describe the concentration of each gas in solution, such that:

$$C_{aq\,i} = k_{Hi} \cdot P_i \qquad (1.2)$$

where each gaseous species will have its respective k_H. In this case, 'i' denotes the partial pressure of each gas in a mixed gas sample.

Additionally, when free phase gas is present, the partial pressure of that gas species as a function of total gas pressure is described by Dalton's Law, where:

$$P_{TDG} = \Sigma P_i \qquad (1.3)$$

In this case, '*i*' denotes the partial pressure of each gas in a mixed gas sample. The partial pressure of each gas species additively is called total dissolved gas pressure, or P_{TDG}. The FPG species composition would be required to determine the contribution of each gas species to P_{TDG}.

Field measurements of P_{TDG} fail to capture the partial pressure of each gaseous species. However, the partial pressure of each gaseous species can be calculated if P_{TDG} measurement is coupled with water sampling and gas analysis methods like gas chromatography. If P_{TDG} is recorded for a sample with a single gas species, then it can be assumed that the measured total dissolved gas pressure is due solely due to that single gas.

1.3.2 Bubbling Point

When dissolved gas pressure exceeds porewater pressure, the gas becomes supersaturated in water. Here, P_{BUB} is defined as the minimum pressure required for P_{TDG} to reach in order for free phase gas (FPG) to exsolve. At the saturation point, P_{TDG} reaches the P_{BUB}, and FPG can be produced. In this case, bubbling pressure is equal to total dissolved gas pressure, such that:

$$P_{BUB\,TOT} = P_{TDG\,TOT} = P_W + P_{CAP} + P_{ATM} + P_{VAP} \quad (1.4)$$

where P_{BUB}, or the bubbling point, is when P_{TDG} is equal to the summation of porewater pressure, capillary pressure, atmospheric pressure, and vapor pressure.

Vapour pressure can be neglected at low temperature (as vapour pressure is low at low temperatures), or when water pressure is much higher than vapour pressure [*Ladd and Ryan*, 2016].

Additionally, atmospheric pressure can be neglected if using gauge pressure in a controlled laboratory system. Discounting these two pressures, the above equation (1.4) can be re-written as:

$$P_{BUB} = P_{TDG} = P_W + P_{CAP} \quad (1.5)$$

It can be seen that P_{TDG} is the pressure applied by the dissolved gas on the water and is opposite to the water pressure acting to collapse the bubble. Additionally, capillary pressure is the force acting between the gaseous and water phases in the system.

Spherical FPG bodies are known as bubbles, however not all FPG bodies are spheres.

1.3.3 Capillary Pressure and FPG

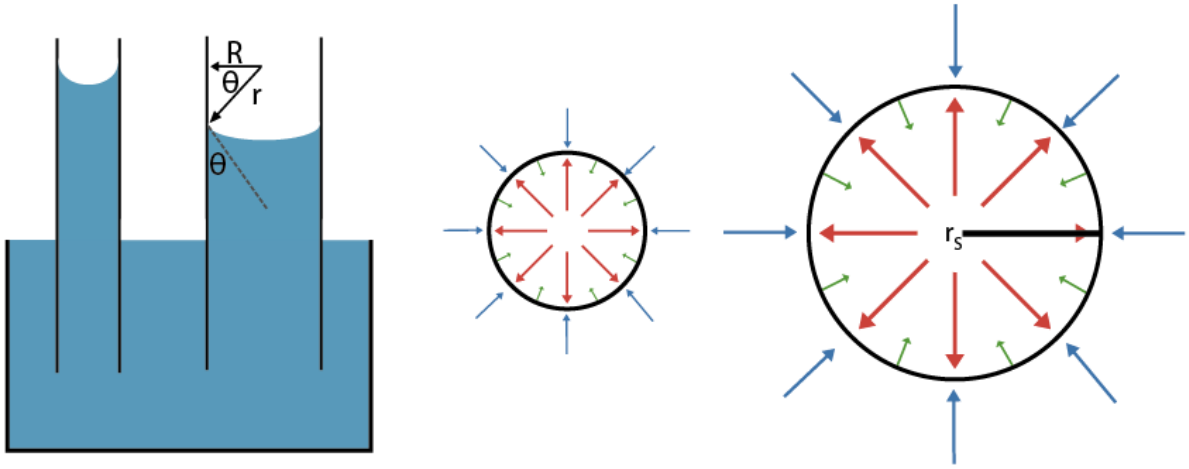

Figure 1.3: Schematic showing the relative the effect of radius on capillary rise in capillary tubes, and the relationship between total dissolved gas pressure, water pressure and capillary pressure in bubbles (figure after *Jury and Horton* [2004]).

Capillary rise in the tubes is a function of intermolecular forces between the water and the glass walls of the tube. Water will rise until the weight of the water exceeds the intermolecular forces between the water and the glass. This balance is a function of tube radius. When comparing the capillary tubes, that with the smaller tube radius has higher capillary pressure, as seen with the height of capillary rise in the narrow tube compared to the larger one (Figure 1.3). In capillary tubes, P_{CAP} is described by:

$$P_{CAP} = \frac{2\gamma \cdot cos\theta}{R} = \frac{2\gamma}{r} \qquad (1.6)$$

where θ is the contact angle between the gas/water interface and surface, and R is the radius of the capillary tube, and r is the radius of the gas/water interface.

Similarly, P_{CAP} of bubbles is inversely proportionate to bubble radius such that:

$$P_{CAP} = \frac{2\gamma \cdot cos\theta}{r^*} \qquad (1.7)$$

where r^* = either:

r_S is the radius of bubble if a bubble is present in a liquid; or,

r_E is the effective radius of pore throat containing the gas/water interface.

From this, capillary pressure for a bubble of a given volume would depend on whether it is present in a free liquid (i.e., not confined in its size by solid phase), or if it being constricted between solid particles or within a fracture, or through a pore throat. It is important to note that if an FPG body is free-floating in a liquid (i.e., not attached to a solid), then the contact angle (θ) is equal to zero (and cos(0) = 1).

In bubbles, P_{CAP} is the difference in P_{TDG} and P_W, and with respect to radius, such that (rearranging equations 1.5 and 1.6):

$$P_{TDG} - P_W = P_{CAP} = \frac{2\gamma \cdot cos\theta}{r^*} \qquad (1.8)$$

1.3.4 Free phase gas and the Ideal Gas Law

When FPG forms in solution, properties of the FPG component are described by the Ideal Gas Law such that:

$$P_{FPG} \cdot V = n \cdot R \cdot T \qquad (1.9)$$

where P_{PFG} is pressure of free gas (Pa), V is volume of occupied FPG (m^3) , n is number of moles of FPG (mol) , R is the Universal Gas Constant (8.314 $m^3 \cdot Pa \cdot K^{-1} \cdot mol^{-1}$), T is temperature (K).

The Ideal Gas Law operates with many assumptions: i) the molecules of gas are small, hard, and spherical, and all collisions are elastic, ii) the distance between the molecules is larger than the size of the molecules, iii) molecules are in constant motion and movement is random, iv) there are no forces between the molecules [*Brady and Senese*, 2009]; however, is still a valid tool to compare the variables for gas species.

Ideally, P_{FPG} could be measured in an FPG body. However, because this is not easily done without comprising the integrity of the FPG body, we use P_{TDG} as a proxy, assuming equilibrium

partitioning between the dissolved and free gas phases. Neglecting capillary effects, P_{TDG} should equal P_{FPG}.

1.4 Soil Water Characteristic Curves (SWCC)

1.4.1 Introduction to SWCC

A SWCC describes the relationship between suction applied to a soil or sediment sample (the independent variable), and the amount of water in the sample (dependent variable) (see example SWCC in Figure 1.4). These two variables can be applied, measured, and reported in different ways. Suction can refer to soil, matric, osmotic, or total suction [*Fredlund et al.*, 2018]. Efforts have been made to describe these relationships using different naming nomenclature [*Fredlund et al.*, 2018]; however, for the remainder of this thesis, SWCC will speak in the general terms of saturation and soil suction.

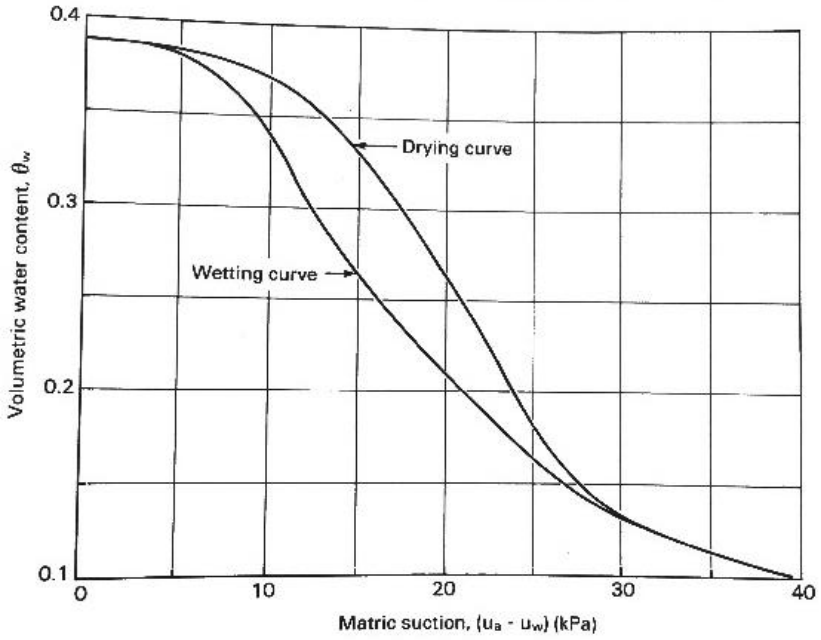

Figure 1.4: Schematic soil water characteristic curve (figure from *Fredlund and Rahardjo* [1993])

SWCC curves were developed in an attempt to better unsaturated soil mechanics, the relationship between air and water pressures in the soil, and soil moisture content [*Fredlund and Rahardjo*, 1993]. SWCCs are also used to provide information for seepage analyses of unsaturated soils [*Rahimi et al.*, 2015a]. Direct measurements of soil permeability is often arduous and costly; however, these values can be estimated from parameters that are derived when SWCC are constructed [*Rahimi et al.*, 2015b]. Relationships between soil suction, defined as the difference between air pressure and water pressure, in addition to soil moisture, are often represented in SWCCs [*Wang et al.*, 2015]. The SWCC is a continuous sigmoidal function that relates water content in a soil to suction [*Azam et al.*, 2013], assuming FPG pressure, or P_{TDG}, is a constant, and is atmospheric pressure. Other names for SWCC include water retention curves or soil retention characteristic curves [*Mahabadi et al.*, 2016; *Fredlund*, 2017].

In saturated soils, hydraulic conductivity is relatively easy to estimate or measure using grain size distribution, and other properties of the soil. However, in unsaturated soils, hydraulic conductivity is a function of water content, which is related to matric or soil suction in a relationship given by SWCC. As such, hydraulic conductivity and permeability can be estimated or modeled from a SWCC as a proxy for direct measurements [*Zhai and Rahardjo,* 2015].

Three distinct sections are typically noted on a SWCC. Starting from initially saturated conditions, these sections can be described as: i) a nearly horizontal component with near complete saturation until the 'air entry pressure' is reached, or where the largest pores begin to be FPG-filled [*Zhai and Rahardjo,* 2012], ii) a steep decline in water content as pores continue to drain (within increasingly smaller pores draining as suction increases), and then iii) a shallowing segment depicting residual saturation (i.e., the amount of water remaining in the sample after the drying ceased), or the amount of water that before considerable suction is required to void the pore space from water [*Azam et al.,* 2013]. The middle segment of typical SWCCs contain an inflection point where the maximum slope is reached [*Fredlund et al.*, 2011]. Past this point, the there is a decrease in amount of water drained from the pores for a given change in suction [*Fredlund,* 2017]. Soils with cracks or fissures can show different slopes on the steep decline portion of a SWCC: the first being for the air entry pressure of air entering the fissure, and the latter for drainage of the pores [*Azam et al.*, 2013].

The steepness of the decline is controlled by the heterogeneity in the pore size, with a narrow pore size having a steeper slope than that of a soil with mixed pore sizes. This can be attributed to soil

microstructure affecting tortuosity, and grain size distribution within the soil [*Azam et al.*, 2013]. The height of the residual water horizontal line is typically attributed to the amount of clay-sized content, or very narrow pore throats where water is adsorbed as the end of suction.

1.4.2 Generating a SWCC

Soil water characteristic curves show the moisture content as a function of the suction applied to a saturated soil (for the desaturation curve). Most commonly in literature, SWCC are generated from laboratory experiments using a pressure plate test where water is suctioned from a saturated sample within a vacuum chamber [*Wang et al.*, 2015]. The amount of water released in response to an applied air suction is measured with increasing suction, and then a SWCC curve is generated from the data. The American Society for Testing Materials (ASTM) has outlined five methods for generating SWCCs, with each method requiring either a hanging column, pressure chamber, volume chamber, chilled mirror hygrometer, and or a centrifuge to generate the vacuum [*ASTM International*, 2008]. Each method has a range of suction pressure that it can operate under, and thus a grain size range that it is optimized for. Essentially, all methods require a sample to be loaded in a sample chamber between two ceramic plates with higher air entry pressures that the sample. Using different methods, suction is applied to a saturated sample, and the amount of water that is drawn out of the sample is measured against the applied suction.

1.4.3 Hysteresis and the SWCC

Up until this point, SWCC have been discussed in the context of water desaturation. However, SWCCs also describe the relationship between suction and water saturation (or re-saturation) of a soil. Complete SWCC showing saturation and desaturation of the same sample shows ‘hysteresis’,

where the wetting and drying curves yield different shapes that are offset at any given pressure (Figures 1.4 and 1.5; [*Pham et al.*, 2005]).

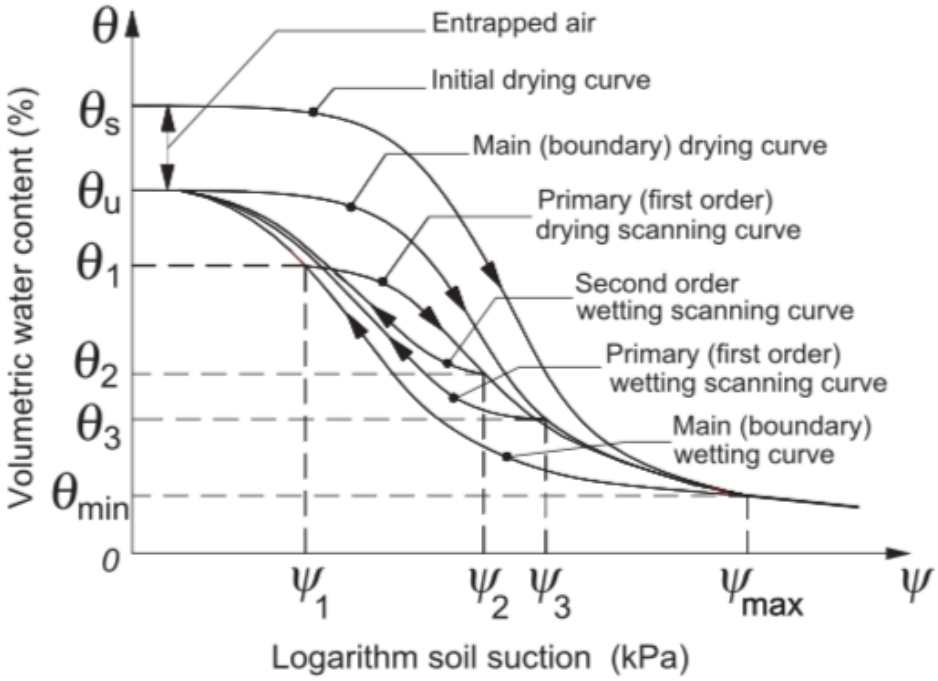

Figure 1.5: Schematic of a SWCC showing hysteresis. Hysteric effects are shown as the scanning curves in between the main drying and wetting (boundary) curves (from *Pham et al.* [2005]).

Specifically, at any given matric pressure, water content is higher for the drying curve than the wetting curve [*Hong et al.*, 2016]. Hysteretic effects are due to a of combination of: i) pore shape irregularities (also referred to as ink bottle effects; [*Hong et al.*, 2016]), ii) differences in menisci shape during saturation and unsaturation, iii) entrapped FPG with re-saturation, and/or iv) sample properties ageing with wetting and drying [*Pham et al.*, 2005]. There are infinite number of scanning curves within a SWCC, but only a few are shown above.

1.4.4 SWCC Modelling

For an unsaturated soil, SWCC can provide insight with regards to permeability and shear strength of a soil [*Fredlund and Xing*, 1994; *Vanapalli et al.*, 1996; *Li et al.*, 2014]. The drying or desorption curve is typically used to estimate permeability [*Fredlund*, 2017]. Many models have been generated to represent SWCC for uniform, bimodal, and well graded soils. Particularities of models have been compared and contrasted, and many model-fitting parameters have been identified to best represent the soil under examination [*Li et al.*, 2014]. Modelling can also predict hysteresis of a soil, within given soil parameters, to minimize experimental time and the costs of generating complete SWCC with hysteresis empirically [*Pham et al.*, 2003, 2005].

1.4.5 Limitation in Applying SWCC to Changes in FPG Content

Previous work in the unsaturated zone mostly deals around near-surface, shallow soil immediately above the groundwater table [*Hong et al.*, 2016]. Similarly, SWCC for unsaturated zones are typically focus on the vadose zone: the area located above the water [*Hillel*, 2004]. However, it is important to consider that unsaturation may be the product of FPG entrapped within pores below the water table. In such cases, it is important to consider the effect of FPG pressure, which is often neglected (as atmospheric pressure, or P_{ATM}) in vadose zone studies. When dealing with entrapped free phase gas bodies, it is important to consider P_{TDG}.

A “quasi-saturated” soil, defined as a partially saturated soil where the FPG is discontinuous, was examined to produce a revised SWCC in a laboratory study by Bicalho *et al.*, [2005]. This experiment resulted in wetting and drying curves showing the relationship between degree of saturation and water pressure. Capillary effects were neglected due to the difficulty of measuring

the radii of individual FPG bodies [*Bicalho et al.*, 2005], and no discussion on FPG formation process are discussed here.

Other published work examines capillary pressure in hydrate-bearing sediment though pore modelling [*Mahabadi et al.*, 2016], however does not explicitly capture the relationship between capillary pressure and saturation at the early onset of hydrate dissociation. Similarly, this early stage relationship was not adequately represented in early FPG formation stages in another group's modelling of free gas from hydrate-bearing sediment [*Jang and Santamarina*, 2014].

1.5 Motivation

Currently, SWCC which describing desaturation from *in situ* FPG production with respect to capillary pressures lack understanding of early FPG exsolution. The purpose of this work is to develop a conceptual understanding of the relation between the *in situ* the production (or consumption) of FPG in initially saturated porous media and relative saturation, or moisture content. Specifically, the relationships between porewater (P_W), total dissolved gas (P_{TDG}), and capillary pressure (P_{CAP}) will be examined to develop a conceptual understanding and revise SWCC to describe *in situ* FPG production.

1.6 Objective

Laboratory experiments were conducted to observe FPG production in an initially saturated specimen. Specifically, this thesis sought to examine:

i) the exsolution and expansion of FPG;
ii) the contribution of capillary pressure in FPG formation and desaturation, and;
iii) the role of dissolved gas diffusion in reaching equilibrium conditions.

This was achieved through laboratory testing whereby a loading cell was packed with uniform-sized glass beads, then saturated with water that was previously saturated with dissolved gas. The pressurized cell then underwent sequential unloading events where relatively small amounts of FPG and water were released into a syringe. After each unloading event, the system was allowed to re-equilibrate. Water content was estimated using dielectric permittivity probe, and P_W, and P_{TDG} were measured throughout this process. This experiment was repeated with different sized glass beads. Lastly, a conceptual and numerical model were created to theoretically understand pressure distribution and gaseous species fractionation throughout FPG formation.

2 METHODS

2.1 Sample Preparation

2.1.1 Bead Separation and Cleaning

For this study, five glass bead sizes were chosen: 2000 μm, 500 μm, 300 μm, 150 μm, and 65 μm. All beads (except 150 and 65 μm) were dried overnight in a 112°C oven for sieving, then sorted using 1000 μm, 710 μm, 590 μm, 500 μm, 300 μm, and 250 μm sieves. The beads soaked in five-molar (5 M) hydrochloric acid ($HCl_{(aq)}$) for three hours, the rinsed with 15 pore volumes of deionized water. The beads were then autoclaved, then re-dried again with the above procedure. The 150 μm and 65 μm beads were purchased as sterilized (https://www.thecarycompany.com/raw-materials/principals/potters and https://www.cospheric.com/, respectively) so did not undergo this procedure.

2.1.2 Porosity and Density Calculations

The porosity of each size range of glass beads was estimated by saturating a known volume of dry glass beads with water and measuring the amount of water added volumetrically and gravimetrically. This resulted in volumetric and gravimetric porosities of the glass beads, as seen in Table 3.1.

Table 2.1: Wentworth soil classification, and lab-derived porosity calculations for the glass beads used in these experiments.

Size range (μm)	Size range (μm)	Soil Classification	Porosity	
			Volumetric	Gravimetric
65	65*	Very fine sand	0.340	0.331
150	150*	Fine sand	0.292	0.309
300	250-300	Medium sand	0.317	0.338
500	300-500	Medium-Coarse sand	0.298	0.310
2000	2000*	Very coarse sand	0.303	0.313

*glass bead sizes are known because they were purchased and/or were in original their containers.

2.2 Loading Cell and the Uniaxial Apparatus

2.2.1 The Loading Cell

The body of the loading cell is a translucent hollow column that is 155 mm in height by 50 mm inner diameter (outer diameter is 75 mm, wall thickness is 12.5 mm, Figure 2.1). Accounting for the space occupied by the top and bottoms platens (30 mm each), the length of the inside of the loading cell, when assembled in the apparatus, is 95 mm, resulting in a total volume of 186.4 mL. The first experiments were conducted in a loading cell constructed of polycarbonate (Lexan), which was replaced by an acrylic (Lucite) cell due to stripping of the threaded ports from over-tightening.

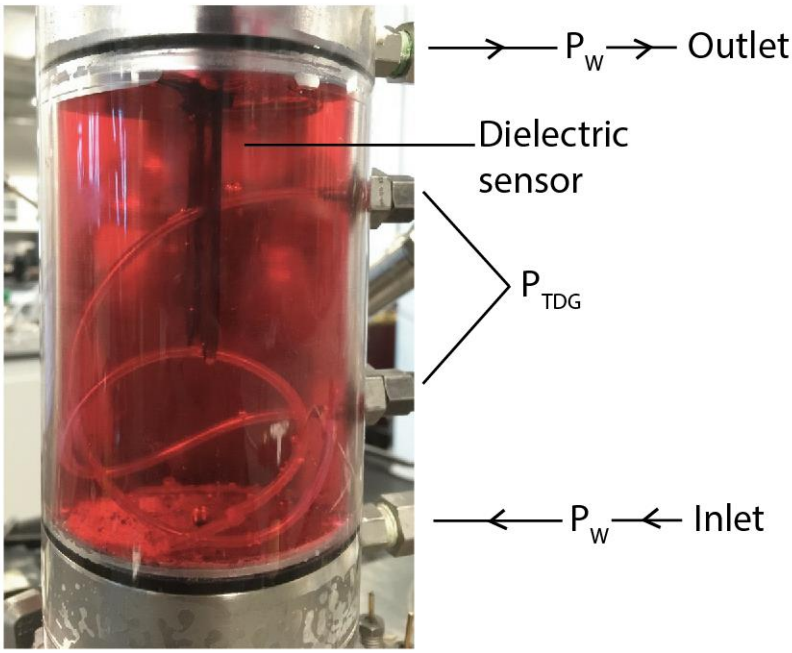

Figure 2.1: Photograph of acrylic loading cell showing the connection to the P_W (top and bottom probes are connected to outlet and inlet bottles, respectively) and P_{TDG} probes (middle two ports), with the silicon tubing attached to the P_{TDG} probes. Here, the loading cell is filled with $CO_{2(g)}$-saturated water that was dyed with red food colouring.

2.2.2 Gas and Water Flow System

Experiments were conducted in a uniaxial apparatus with constant principle normal stress. The loading cell was connected to the inlet bottle through a bottom port to ensure slow saturation of the glass beads with minimal FPG trapping when the loading cell was filled prior to each experiment. The top of the loading cell was connected to a stainless-steel line (1.5875 mm or (1/16-inch) diameter) that was connected to the outlet bottle (Figure 2.2). Porewater pressure (P_W) was measured at both the connection between the loading cell and both its inlet (referred to as the P_W lower) and outlet (P_W upper). The total dissolved gas pressure (P_{TDG}) probes were located at one-third and two-thirds of the cell height.

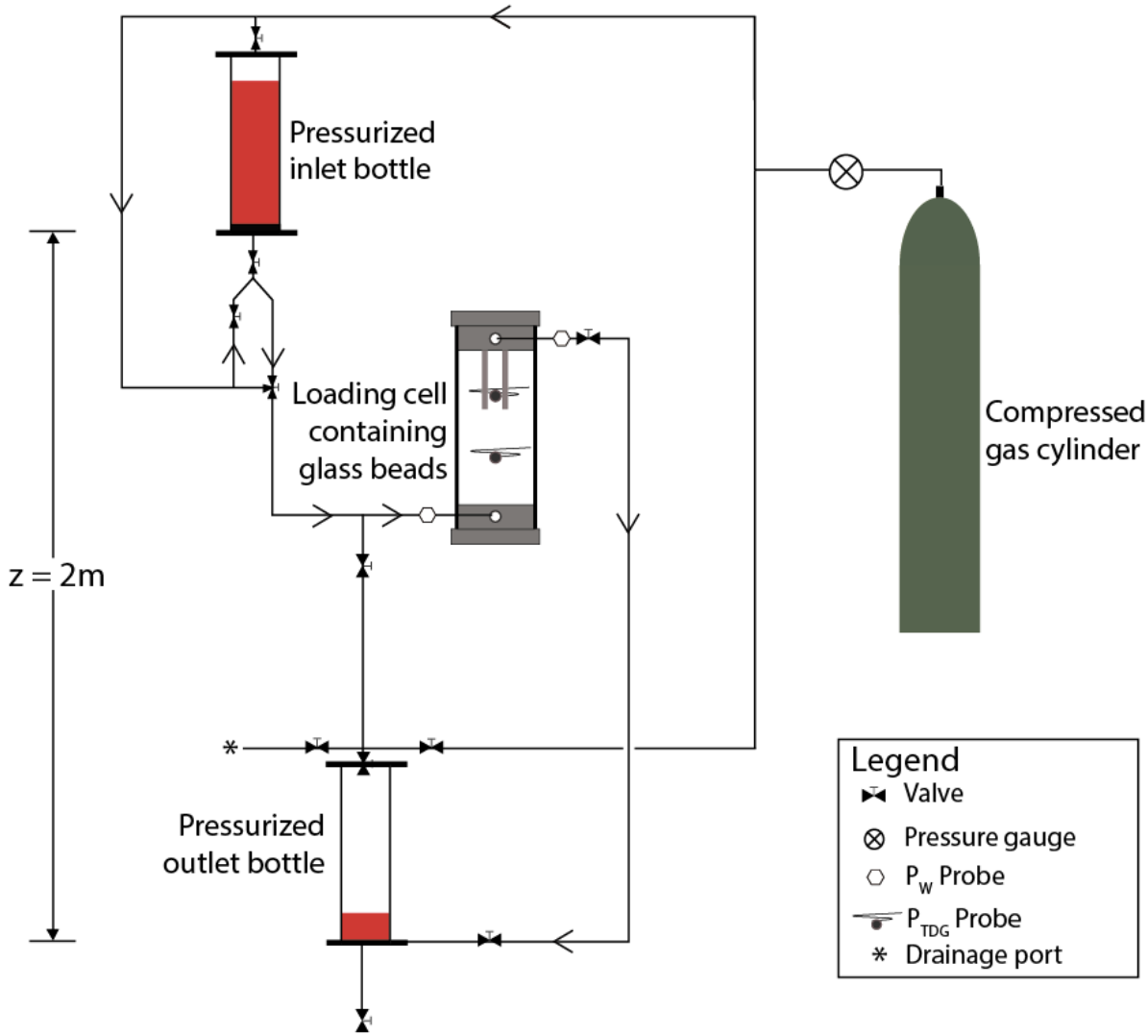

Figure 2.2: Schematic diagram showing the flow system of the experimental setup including CO_2 gas cylinder, inlet and outlet bottles, and loading cell. The CO_2 gas cylinder is connected to the bottle of the inlet bottle (to gas-saturate the water), as well as to the loading cell and outlet bottle. Inlet and outlet bottles are separated by a two-meter elevation difference. Inlet bottle is connected to the bottom of the loading cell (passing through the lower P_W probe), and the loading cell drains to the outlet bottle through the top of the loading cell (passing through the upper P_W probe). There is a line of tubing from the bottom of the loading cell that is connected to a valve that acts as the drainage port during unloading events. A photograph of loading cell showing the inlet of P_W (top and bottom ports of middle figure) and P_{TDG} probes (middle two ports of middle figure), and the silicon tubing (cannot be seen) attached to the P_{TDG} probes.

The bottom of the loading cell is also connected to a 62 cm-long (two mm- thick) piece of tubing. The other end of this tubing has a Swagelok valve connected to a six cm piece of stainless-steel tubing, with internal volume of 1.84 mL. This small piece of tubing is the 'drainage port' where sample was unloading at each step of the experiment (Figure 2.2).

2.3 Pressure Probes and Moisture Content Measurement in the Loading Cell

2.1.1 P_W Probes

Two types of porewater pressure (P_W) probes were integrated in the loading cell and connected to external data logging units which recorded pressures every five seconds. The upper P_W probe was an Omega probe (https://www.omega.com/section/pressure-transducers.html), connected to an external laptop. The lower P_W probe was a Honeywell 'AB High Performance' probe (https://sensing.honeywell.com/sensors/pressure-sensors-transducers). Both probes collected data every five seconds throughout the experiments. Calibration of the P_W probes was checked before each experiment by comparing the measured P_W with using compressed CO_2 gas pressure as read on the gas regulator.

2.1.2 P_{TDG} Probes

The P_{TDG} probes were constructed as described by Roy and Ryan [2013] using Honeywell 'AB High Performance' pressure transducers (same as above) connected to the outside of the loading cell by 3.175 mm (1/8-inch) Swagelok valves via 1.5875 mm (1/16-inch) hollow stainless-steel tubing. The opposite end of the stainless-steel tubing to the probe (i.e., inside the loading cell) were sanded to a taper and fitted with a 17 cm length of silicon tubing on the inside of the loading

cell which was changed between every experiment to reduce effects of biofilm accumulation). The P_{TDG} probes were connected dataloggers which recorded P_{TDG} data every second. Calibration of the P_{TDG} probes was conducted in the same fashion as the P_W probes, with the stainless-steel tubing connected directly to the compressed gas regulator before each size range of glass beads was tested.

2.1.3 Dielectric Sensor Probe

Using an ECH$_2$O® EC-5 (https://www.metergroup.com/environment/products/ec-5-soil-moisture-sensor/), soil moisture content was estimated throughout the experiments. This probe measures the bulk dielectric permittivity of the soil to then yield a volumetric water content (VWC). Water saturation was then estimated by exploiting differences in dielectric permittivity in air, soil (bead), and water fractions to ultimately determine the volume fraction of water in a sample. The ECH$_2$O probes was built into the upper platen that would be the 'lid' of the loading cell, as seen in Figure 2.3.

Figure 2.3: Photograph of the top platen of the loading cell constructed of polycarbonate (Lexan). The bottom of the platen houses the ECH$_2$O EC-5 Dielectric sensor probe (. prong length is 5 cm). Also photographed are the O-ring (to ensure the loading cell is sealed shut), and the threaded port to connect the loading cell to the outlet bottle.

The VWC values were then converted to a saturation using the porosity of the grains, as seen in Equation 2.1.

$$Saturation\ (\%) = \frac{VWC}{Porosity} * 100\% \qquad (2.1)$$

Data were acquired every five seconds on an external laptop through a datalogger. This probe has an ideal measurement volume of 300mL [*Decagon Devices Inc.*, 2016].

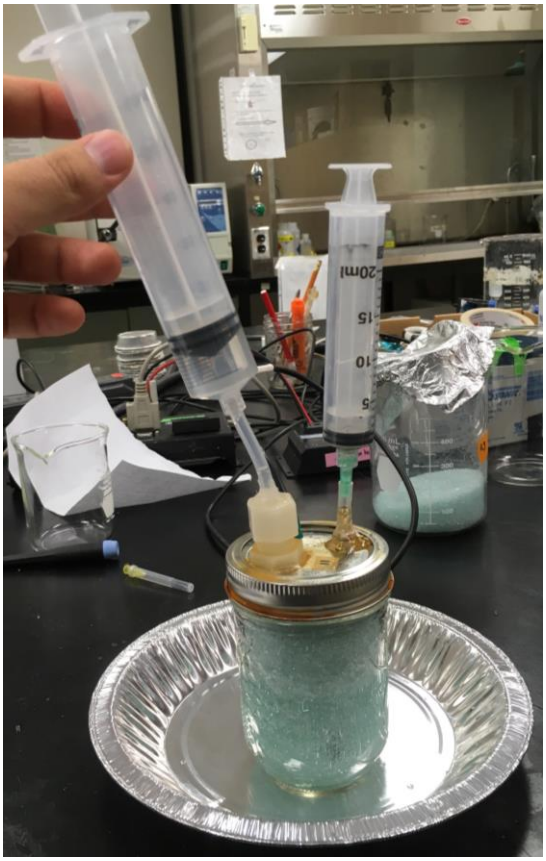

Figure 2.4: Photograph of the dielectric sensor probe calibration vessel made from a glass Mason jar. Lid of the mason jar is equipped dielectric sensor probe, and with two fittings each with silicon septa, and two syringes, (for injection and evacuation). Known amount of FPG was injected in the sample in discrete FPG bodies (right syringe) as water was pushed out of sample into left syringe. Mason jar filled with 500 μm glass beads here.

Being a field probe, it was expected that the most accurate measurement is for uniform desaturation from the top. In this experiment, initial desaturation would arise from FPG formation. As such, as calibration vessel was constructed using a Mason jar with water injection and air ejection ports (Figure 2.4). As water was injected from one syringe into the Mason jar, air was evacuated into the other syringe. Water injection occurred in increments, with the syringe being pulled out slightly each time. The intention was to leave small, discrete FPG bodies and detect changes in VWC. Saturation values were compared between those determined by the amount of water injected versus those calculated from the VWC output from the dielectric sensor probe. This procedure continued

until the injection of water lead to the ejection of water already in the Mason jar. This occurred sooner for the smaller glass beads. Unfortunately, the presence of isolated discrete FPG bodies within the sample could not be visualized through the Mason jar.

2.4 Experimentation

2.4.1 Experimental set-up

One day prior to commencing an experiment, the inlet bottle was disconnected from the system, washed with water and 10% bleach to clean of any biofilm growth, then filled to 80% volume with tap water. A magnetic stir bar, red food colouring (to help with visualization within the loading cell), and sodium azide (0.01%, bacteriocidal to help prevent biofilm growth; [*Lichstein and Soule*, 1943]) were added to the inlet bottle. The inlet bottle was subsequently hooked up to the uniaxial system and the in-house vacuum, and then stirred (using a magnetic stir plate) for three hours in order to de-air the water. After the vacuum was removed, water in the inlet bottle was saturated with ca. 650 kPa of compressed $CO_{2(g)}$ via a porous stone at the bottom of the inlet bottle overnight to ensure the inlet water was $CO_{2(g)}$-saturated. Approximately one hour into the $CO_{2(g)}$-saturation process, the headspace of the inlet bottle was purged briefly to allow for the escape of any residual non-$CO_{2(g)}$ gases. Carbon dioxide gas was used for these experiments due to its safety and rapid diffusion through silicon tubing (i.e., high diffusivity constant) [*Cadogan et al.*, 2014].

A piece of 40 μm Nitex® nylon fabric (woven mesh, http://www.dynamicaqua.com/nitex.html) was placed at the bottom of the loading cell to prevent glass beads from plugging or escaping through the drainage port (3.5 mm diameter) located on the bottom platen. The glass beads were

then moistened with tap water (to approximately 5% by weight) and added in increments into the loading cell using a moist tamping technique to facilitate even packing. The silicon tubing was coiled at the same height of the P_{TDG} connection such that it did not touch the wall of the loading cell. A similar piece of nylon fabric was placed under the upper platen in order to prevent glass beads from entering and plugging the port at the bottom of the top platen. After the upper platen was placed on top of the cylinder, a cross bar was mounted on top of the upper platen and fixed to the base of the loading cell using built in nuts and bolts.

The system was then purged with compressed $CO_{2(g)}$ to remove any atmospheric gases prior to loading with $CO_{2(g)}$ saturated water from the inlet bottle. The loading cell and outlet bottle were then pressurized to the same pressure as the inlet bottle using pressurized $CO_{2(g)}$ gas that was connected directly to the inlet and outlet bottles. Next, the loading cell was slowly saturated with $CO_{2(g)}$-saturated water. At this point, the inlet bottle, loading cell, and outlet bottle are pressurized to the same $CO_{2(g)}$ pressure (or CO_2-saturated water pressure in the case of the inlet bottle), as regulated from the $CO_{2(g)}$. The saturation of the loading cell occurred as the CO_2-saturated water flowed from the inlet bottle, upwards through the loading well, and then outwards through the top of the loading cell. This process often took up to four hours as flow was only controlled through elevation head difference ($\psi = 0$, z = 2 m, so h = 2m, see Figure 2.2,). If saturation seemed to have stopped (by observing the dyed water level height in the loading cell had stopped moving), small amounts of $CO_{2(g)}$ were released from the top of the outlet bottle to the atmosphere encourage flow. In this case, flow was also driven by a pressure head difference of approximately 5 kPa (now ψ = 0.5, z = 2 m, so h = 2.5 m) because the PFG pressure in outlet bottle was reduced to 5 kPa less than that of pressure of loading cell and inlet bottle. When the system reached at least 98%

saturation (as measured by the dielectric probe, the loading cell was isolated from the inlet and outlet bottles by what kind of valves. Once the P_W and P_{TDG} probes equilibrated, the experiments began. The experiments were hydrostatic (i.e., loading cell was isolated from inlet and outlet bottles, so no water or $CO_{2(g)}$ flow).

2.4.2 Experimental Procedure

Each experiment was performed with only one of the five grain sizes in the loading cell (or no grains for the control experiments) and started at initial P_W and P_{TDG} values of approximately 650 kPa. This was achieved by filling the loading cell with CO_2-saturated tap water at an elevated pressure via the compressed gas cylinder, and allowing the P_{TDG} probes to equilibrate before the loading cell was saturated with the gas-saturated water. Once loaded with CO_2-charged water, the sample volume was confined by the apparatus, which resulted in net confining stress of the gas-saturated water.

Each experiment consisted of a series of sequential unloading 'events', each of which drained the system incrementally, and cause the exsolution of FPG in an initially saturated loading cell. The sequential unloading events were conducted until the loading cell reached at atmospheric pressure. Each unloading event consisted of sequential unloading of 1.84 mL sample ($CO_{2(g)}$ and water) by connecting an empty 60mL lubricated syringe to 'drainage port' attached at the outlet of the loading cell apparatus. The syringe barrel was lubricated with grease and emptied, then compression-fitted to the drainage port. The water and FPG phases in the syringe were measured. The system then recovered (i.e., when the P_W and P_{TDG} probes came to equilibrium) before the next unloading event. This procedure was repeated until the system reached approximately 70%

saturation, then unloading continued with double the amount of volume removed per unloading event. The 'earlier' unloading events had less volume in order to yield finer-resolution data at high saturations. Unloading continued until the system was either drained of water, or until the loading cell reach atmospheric pressure (or zero-gauge pressure).

2.4.3 Data Collection and Analysis

Due to the time-intensive process of setting up the experiment, often requiring repeated assembly and disassembly of the apparatus to ensure airtightness, earliest data were removed from the figure.

This procedure was repeated multiple times per grain size until complete experiments (i.e., from initial P_W and P_{TDG} gauge values of ca. 650 kPa, and final gauge values of ca. 0 kPa) data were complete for two or three experiments. Among other calculations, the P_W and P_{TDG} values at each unloading event were divided by the initial P_W and P_{TDG} values for that given experiment as a way to normalize the experiments as they continued. This was to ensure some way of comparing experiment to each other, as initial P_W and P_{TDG} were difficult to control within a few kPa for consistency across all experiments.

Data from P_W, P_{TDG}, and VWC measurements were then collated and analyzed in Microsoft Excel and MATLAB. Data from each unloading event in the successful experiments are shown in Appendix A1.

3 RESULTS AND DISCUSSION

3.1 P_W and P_{TDG} Rebound

Each unloading event yielded a similar response in water and dissolved gas pressures (Figure 3.1). Each experiment, which consisted of a series of unloading events, started at quasi-equilibrated P_W and P_{TDG} pressures, with P_W and P_{TDG} within ca. five kPa of each other.

A rapid decline in P_W was observed immediately after each unloading event was initiated (i.e.as a gas- water mixture was released into the syringe). Upon unloading, the instantaneous reduction in P_W below P_{TDG} (to a minimum value called P_{MIN}), caused gas supersaturation in the water, and thus FPG exsolution [*Wong and Maini*, 2007]. The initial, maximum drop in P_W is denoted as P_{DROP} (Figure 3.1). The P_W 'rebound', where P_W was due to FPG growth, where the FPG body contributed to porewater pressure by growing outwards into the aqueous phase. The lost P_W, or the difference in P_W values after and just prior to each unloading event was denoted as non-recoverable pressure (P_{NR}).

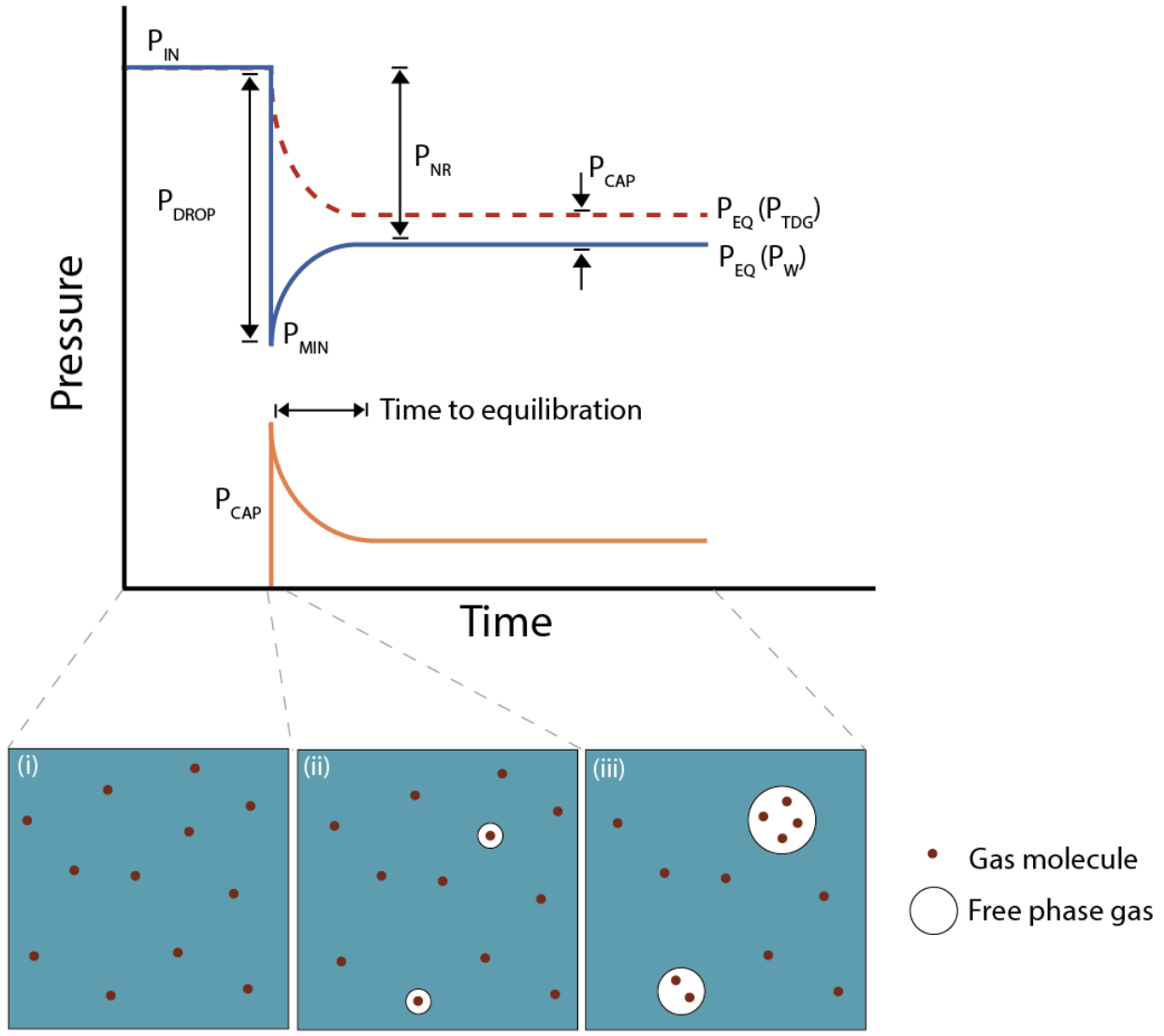

Figure 3.1: Schematic describing the response of water pressure (P_W) and total dissolved gas pressure (P_{TDG}), and calculated capillary pressure (P_{CAP}) with time during one unloading event. Prior to unloading, the P_W and P_{TDG} values are equilibrated to an initial pressure (P_{IN}). The P_W value then decreases by P_{DROP}, reaching minimum value of P_{MIN}. Nonrecoverable pressure is noted at P_{NR}, and both P_{TDG} and P_W reach new equilibrium. P_{CAP} is estimated the difference of the P_W and P_{TDG} curves, and the orange line. Time to equilibration is the time between P_{MIN} and the re-equilibration pressures (which are the P_{IN} for the subsequent unloading event). Bottom panels indicate gas species (red dots) (i) dissolved in water, (ii) partitioned into FPG right after FPG nucleation coinciding with the drop in P_W, and (iii) diffusing into FPG until equilibrium is reached.

Recovery in P_W was slower than P_{DROP}, and this is due to the interdependence between diffusion and gas partitioning from the aqueous to the free gas phase. The processes associated with each unloading event are summarized in the following list as an overview, and are to be expanded on in sections to follow:

1. P_W is decreased to P_{MIN} during P_{DROP}, causing decreased P_{BUB},
2. P_{TDG} exceeded P_{BUB}, resulting in the exsolution of dissolved gas into FPG,
3. This partitioning of dissolved gas to FPG caused a lowered P_{TDG} (governed by Henry's Law, and only for a single species),
4. Time dependence of P_{TDG} decrease is a function of time it takes dissolved gas to diffuse through water so that it partition into FPG (governed by Fick's Law),
5. Gas partitioning continues until Henry's and Fick's Laws are satisfied, and P_{CAP} is minimized, with P_{CAP} decreasing as FPG bodies increase in size.

Time to equilibration is controlled by three inter-dependent processes: i) the diffusion of dissolved gas to FPG, ii) dissolved and FPG pressure distribution to satisfy Henry's Law coefficient (the proportionality constant between a pressure and amount of dissolved gas, Equation 1.2), and iii) Ostwald ripening effects and the minimization of P_{CAP} (Figure 3.1). Since there is only one gas species (i.e., $CO_{2(g)}$) in the system, the change in P_{TDG} is directly proportional to the partial pressure of CO_2 (P_{CO2}, equation 1.2), hence the partitioning of dissolved gas into FPG will occur until Henry's Law constant is satisfied. Additionally, movement of gas is driven by a concentration gradient (diffusion), as well as thermodynamic, as a two-bubble system is less thermodynamically stable than a single bubble system [*de Chalendar*, 2016]. The lower panel of Figure 3.1 illustrates: (i) no FPG initially, and all gas species in the dissolved phase, (ii) the onset of FPG forming at the

unloading event to satisfy Henry's Law, and (iii) gas partitioning to the free gas phase, leaving a small area of gas-depleted water around each FPG body which will then drive diffusion (according to Fick's Law). While the interplay of these three processes are complex, having a mixed-gas species (as is commonly found in groundwater) would complicate this system even further.

The decrease seen in P_{TDG} often required more time to reach a new equilibrium. This was likely due to time required for the gas to diffuse through water [*Wong and Maini*, 2007] and the silicon tubing attached to the P_{TDG} probes into the system [*Manning et al.*, 2003].

Once the P_W and P_{TDG} values reached new P_{EQ} values, another unloading event was conducted. This process was repeated until the loading cell either reached atmospheric pressure (i.e. P_W was zero), or until free water was no longer released.

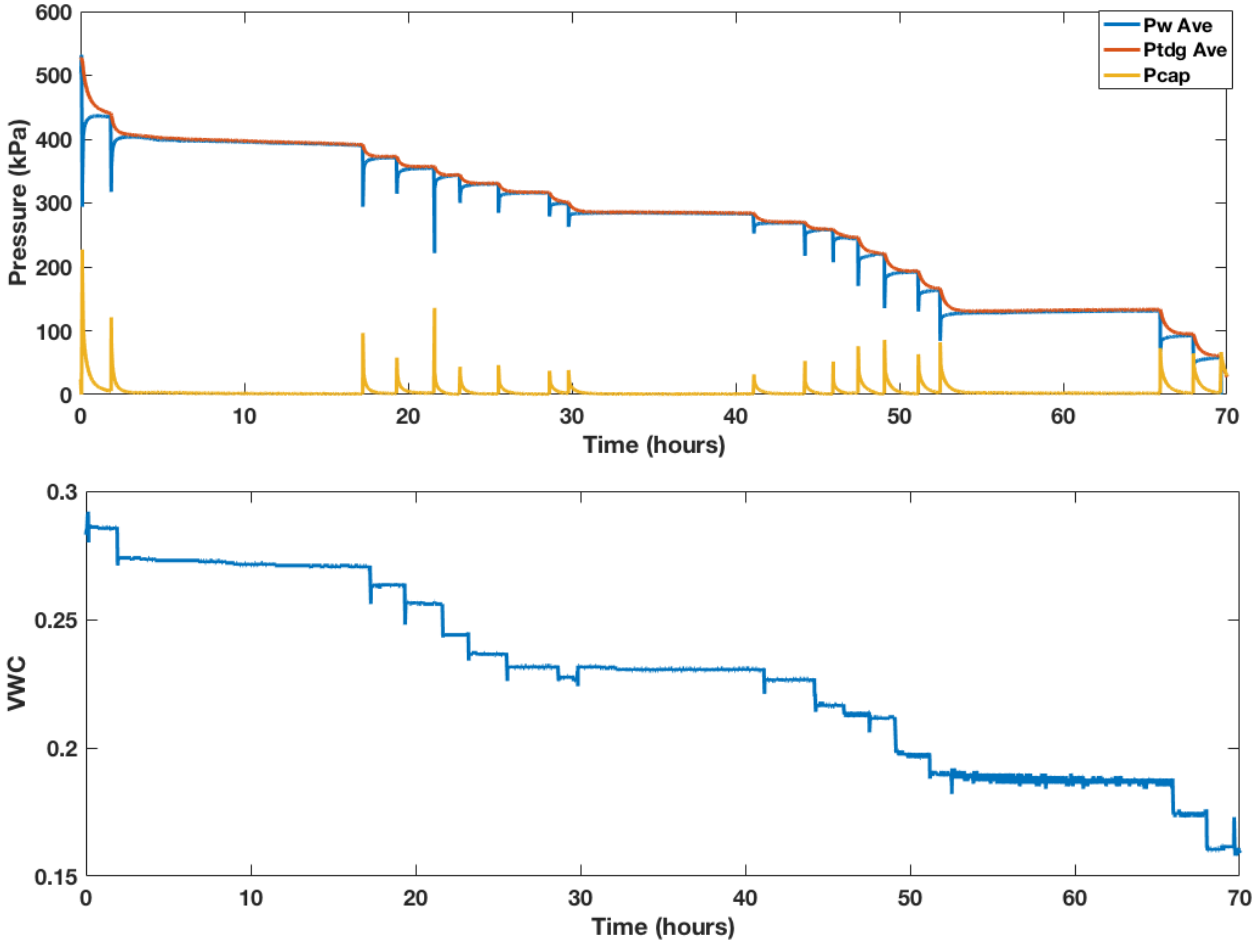

Figure 3.2: Sample data showing the entirety of unloading experiment for 150 µm beads. Upper figure shows P_{TDG} (red line), P_W (blue line), and calculated P_{CAP} (orange), and lower figure shows VWC data. Experiment started at ~550 kPa, and each unloading event is denoted by the dramatic decrease in P_W (18 events seen here). Long flat portions in P_W and P_{TDG} indicate hiatuses in data collection and demonstrate integrity of flow system. P_{CAP} was calculated as the difference between P_{TDG} and P_W.

A set of sequential unloading events for the 150 µm glass beads is shown in Figure 3.2 (with the remaining datasets in Appendix A2). Of note in the data are the long (~10 hour) lags in the experiment, representing the overnight periods between the experiment days. The stable and flat values of these time periods are indicative of an airtight loading cell void of leakage, which is essential in this type of experiment. In each unloading event, the P_W and P_{TDG} had reached

equilibrium values, then at unloading, the P_W decreases drastically with the evacuation of gas-saturated water. The P_W then recovers gradually before plateauing and reaching a new equilibrium value. The P_{TDG} slope also approaches zero and P_W and P_{TDG} are once again in equilibrium (approximately two hours). This process was repeated over several days until the loading cell either reaches atmospheric pressure (i.e., P_W is 0 kPa), or until there was no water left in the system to drain.

3.2 Free Phase Gas Volume Increase and during Sequential Unloading

Various stages were visually observed throughout repeated unloading events, independent of the grain size in the loading cell as are described in Figure 3.3. In every instance, the experiment would start at near-complete water saturation (≥ 97%, see Equation 2.1) with all gas present in the dissolved phase and no visible FPG bodies. Visually evident macroscopic FPG bodies formed or 'nucleated' after the first unloading event. With sequential unloading events, the FPG body size grew to a point that they would occupy one pore space, then invade multiple pore spaces. Finally, these larger FPG bodies ultimately migrated upwards, forming a headspace, or FPG cap, in the loading cell. These steps in FPG formation and growth are described in more detail in the following sections. Additional FPG bodies would form in early unloading events that followed the initial unloading event and were not limited to the first unloading event.

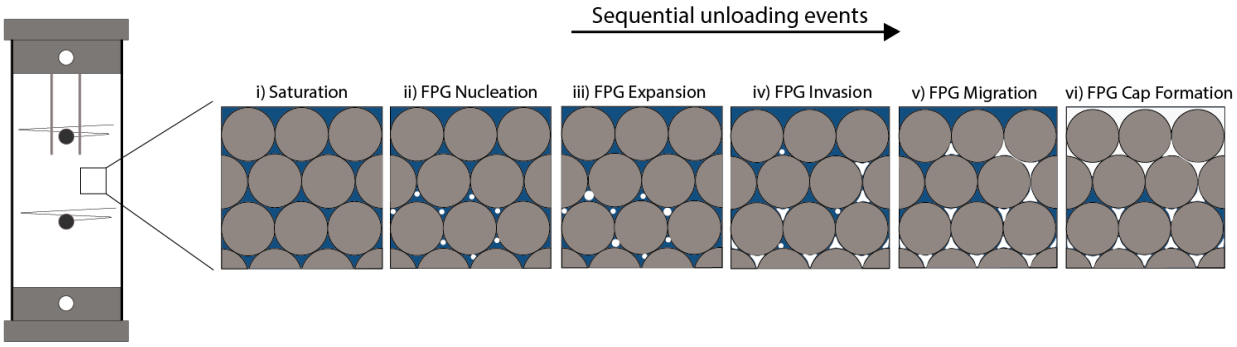

Figure 3.3: Schematics depicting the stages of FPG formation and growth that were visually observed throughout sequential unloading in each of the experiments. Stage i) indicated no FPG present, and water is gas-saturated, ii) shows FPG nucleation, iii) demonstrates the growth of the nucleated FPG bodies, iv) shows the invasion of FPG into multiple pore spaces, v) shows upwards movement of FPG, and vi) the formation of an FPG gas cap at the top of the sample. Bubble nucleation here represents the earliest time when bubbles were visually observable.

3.2.1 Free Phase Gas 'Nucleation'

Free phase gas nucleation is referred to as homogenous or heterogenous [*Jones et al.*, 1999; *Bauget and Lenormand*, 2002; *Boudreau*, 2012]. Homogenous nucleation is the formation of FPG bodies in a single phase, and requires higher levels of supersaturation than heterogeneous since it is thermodynamically more demanding [*Bauget and Lenormand*, 2002; *Nejad et al.*, 2005; *Boudreau*, 2012]. Conversely, heterogenous nucleation is catalysed by a sudden supersaturation of the dissolved phase in solution [*Jones et al.*, 1999]. Both homogenous and heterogeneous nucleation theories are considered 'classic' as they are based on thermodynamic equations governing the threshold energy required to create a FPG body, and both theories require a high activation energy to overcome the energy barrier of forming FPG in a liquid phase [*Jones et al.*, 1999]. A third type of nucleation, referred to as 'pseudo-classical nucleation' occurs when FPG bodies form from pre-existing microbubbles (or seeds) within the solution, on particle surfaces, or in pre-existing gas cavities [*Jones et al.*, 1999]. In this case, pre-existing bubble seeds are of radii

smaller than the critical radii of bubble formation, where the critical radius is the minimum radius required for thermodynamically stable FPG to form. This then requires a lesser activation energy for FPG nucleation [*Jones et al.*, 1999]. Pre-existing seed bubbles, surfactant, and/or wall or grain roughness can provide stable locations for bubble FPG and growth due to capillary effects [*Bora and Maini*, 1997; *Jones et al.*, 1999; *Bauget and Lenormand*, 2002]. Essentially, these surfaces act as catalysts to reduce the activation energy required for FPG nucleation [*Jones et al.*, 1999]. In this experiment, FPG bodies were like formed by 'pseudo-classical nucleation', where microscopic pre-existing FPG bodies or residual surfactant acted as the seeds for the macroscopic FPG to form. In the experiments described in this thesis, FPG nucleation did not only occur after the initial unloading event; rather, FPG bodies continued to nucleate in subsequent early unloading events.

3.2.2 Free Phase Gas Expansion

Free phase gas nucleation is followed by growth or expansion. While FPG nucleation is a rapid process that can occur after the reduction of P_W, expansion occurs over a longer time period. FPG bodies grow through mass transfer by the diffusion of dissolved gas into the free gas phase [*Wheeler*, 1988; *Bauget and Lenormand*, 2002]. Molecular diffusion is governed by Fick's First Law:

$$J = -D \cdot \frac{dC}{dx} \qquad (3.1)$$

where J is the diffusive flux ($mol \cdot L^{-2} \cdot s\text{-}1$), D is diffusivity ($m^2 \cdot T^{-1}$), C is concentration ($mol \cdot m^{-3}$), and *x* is position (m).

Fick's First Law describes the diffusive flux that occurs due to concentration gradients in one dimension (in the above equation). Inherent in this equation is a concentration gradient, where

diffusion occurs from areas of high concentration to low concentration. Diffusivity is a constant for a gaseous species at a given temperature.

The rate of diffusion controls the rate of FPG expansion, ultimately controlling the time for P_W rebound (assuming portioning at FPG-water interface is fast), which is a function of diffusion time, FPG body size, and density of FPG bodies [*Wong and Maini*, 2007]. Over the course of unloading events in each experiment, the rebound time (Figure 3.1) decreased, indicating that FPG bodies have reached equilibrium size more quickly. This decrease in recovery time is due to the increase in the amount of space that is FPG-occupied (i.e., decreased water saturation), so the dissolved gas had less volume of water to diffuse through to reach the free phase gas.

Diffusion is not the only process controlling gas partitioning. Henry's law relates gas pressure to the concentration of the gas by a proportionality constant (Henry's constant, k_H). Partitioning of gas species from smaller FPG bodies to larger FPG bodies is towards a more thermodynamically stable state [*de Chalendar*, 2016]. This process, where the expansion of larger FPG bodies is at the cost of the shrinkage and eventual collapse of smaller FPG bodies, is known as Ostwald ripening [*Naber et al.*, 2008; *de Chalendar et al.*, 2018].

If the FPG bodies are suspended in the liquid phase (i.e., not trapped between glass beads or the loading cell wall), then $r = r_s$ (where r_s is radius of the bubble sphere)

$$P_{CAP} = \frac{2\gamma \cdot cos\theta}{r_s} \qquad \text{(recall 1.7)}$$

In this case, capillary pressure is controlled by FPG radius, where larger bubbles have lower capillary pressures (recall Equation 1.7). This inverse relationship means that smaller bubbles have larger capillary pressures. Consequently, bubble growth in the early phases of unloading is accompanied by decreasing capillary pressures throughout the experiments.

3.2.3 Free Phase Gas Invasion

If FPG volume increases, it will reach a point where a pore space is effectively occupied by FPG (neglecting for residual water film on the solid phase). With prolonged FPG volume growth, from diffusion or FPG production, FPG can invade multiple pores, completely surrounding a grain or few grains of the matrix; a process commonly referred to as invasion percolation or capillary invasion [*Boudreau*, 2012], however this process will be referred to here as PFG invasion.

Once an FPG body completely invades one pore, the radius of the FPG body is constrained by the pore throat radii. Now, capillary pressure is such that $r^* = r_E$ (r_E is the effective radius of the pore throat, see Equation 1.7):

$$P_{CAP} = \frac{2\gamma \cdot cos\theta}{r_E} \qquad \text{(recall 1.7)}$$

In this scenario, capillary pressure is governed by the effective radius of the pore throat. As FPG invades, it must squeeze through a pore throat that narrows due to geometry and packing of spherical glass beads. This decrease in pore throat radius results in an increase in capillary pressure.

It is important to distinguish the effect that the radius can have on capillary pressure. During FPG expansion, a growing FPG body has a decreasing capillary pressure. In invasion however, a growing FPG can show increased capillary pressure as it invades through narrow pore throats [*Mumford et al.*, 2009]. Additionally, due to high capillary pressures associated with smaller pore throats, the larger pore throats desaturate first [*Furbish*, 1997].

Previous studies have found that FPG will preferentially occupy specific pore or fracture networks prior to invading multiple pores, but this is a function of the pre-existing pore and fracture networks [*Boudreau*, 2012]. In compressible and low strength materials, continued FPG generation would result in elastic or plastic deformation of the of the matrix [*Wheeler*, 1988; *Boudreau*, 2012], depending on the properties of the sediment. However, this was not the case in the examined experiments due to the relative incompressibility of the glass beads.

3.2.4 Free Phase Gas Migration

Following the FPG invasion of multiple pores, the FPG can migrate upwards [*Bauget and Lenormand*, 2002]. In this work, this upward migration is termed FPG migration, and results in the formation of an FPG "cap" at the top of the sample (see Figure 3.3), similar to a headspace in a water sample. Migration upwards is favoured due to a decrease in hydrostatic pressure as water was evacuated during unloading events [*Mumford et al.*, 2009].

As the FPG body increases in volume under constant P_W, it's buoyancy force also increases (Figure 3.4).

Buoyancy force is given by:

$$P_{BUOY} = (\rho_W - \rho_{FPG}) \cdot g \cdot h_{FPG} \qquad (3.2)$$

Where P_{BUOY} is buoyancy pressure (kPa), ρ_W and ρ_{FPG} are the densities of water and FPG, respectively, g is gravitational constant (9.81 m $\cdot s^{-2}$), and h_{FPG} is the height of the FPG body.

Before the FPG body can migrate, it must overcome an energy barrier of a pore throat.
Each pore throat acts as a barrier that must be overcome in order for the FPG to migrate through it. This barrier requires a certain exit pressure threshold, or P_E, to be met in order for the gas to invade through it.
And pore exit pressure, or capillary pressure:

$$P_E = P_{CAP} = \frac{2\gamma \cdot cos\theta}{r_E} \text{ (recall 1.7)}$$

The exit pressure, P_E, is generated from the interfacial tension of the FPG body and the pore throat walls [*Furbish*, 1997; *Chen and Slater*, 2015]. Because P_E, like P_{CAP}, is inversely proportional to radius, and FPG will leave through the largest adjacent pore.

There has to be enough FPG present at a given water pressure such that the height of the FPG body is enough for the buoyant force to overcome the restricting pore throat exit pressure. As such, these equations can be rearranged such that:

$$h_{FPG} = \frac{2\gamma \cdot cos\theta}{(\rho_W - \rho_{FPG}) \cdot g \cdot r_E} \qquad (3.3)$$

Where ρ_W and ρ_{FPG} is the density of water and PFG, respectively, g is the gravitational constant.

In DNAPL (Dense Non-Aqueous Phase Liquid) literature, the pool height is the minimum required height for a DNAPL to overcome entry pressure of a fracture [*Pankow and Cherry*, 1996]. In the case of FPG migration, the minimum pool height is the value required for the FPG body to migrate upwards through the largest pore throat. In this equation, the effective radius, r_E, is that largest pore throat adjacent to the FPG body, and the FPG body exits through the largest throat because it has the smallest exit pressure (P_E).

When this buoyancy exceeds the limiting pore-throat exit pressure, the FPG body can escape through this pore and will migrate until the volume of the residual FPG body is such that the buoyancy no long exceeds the limiting pore throat exit pressure.

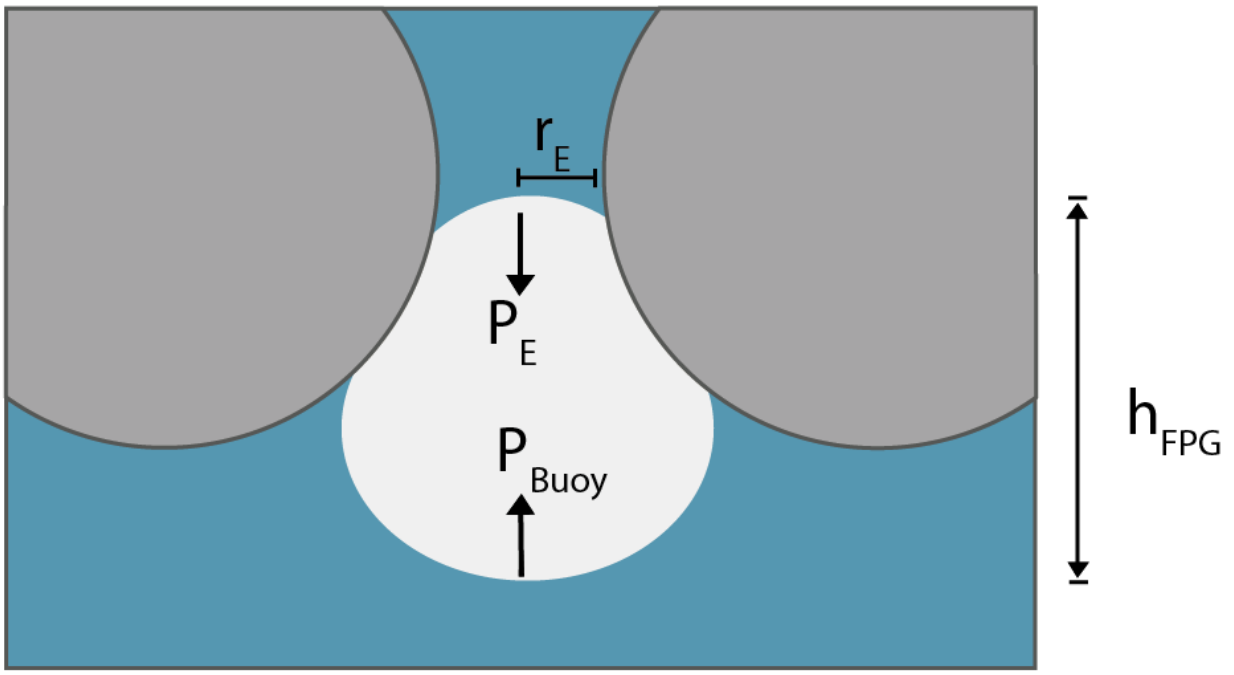

Figure 3.4: Schematic of the forces involved in FPG migrating upwards through a pore throat (existing between two grains or glass beads). FPG body of a given height, h_{FPG}, will migrate upward when buoyance force (P_{BUOY}) exceed the exit pressure (P_E) from the small pore throat of radius (r_E). Figure modified from *Chen and Slater* [2015].

FPG migration can be either continuously produced (from microbial processes, for example), or discontinuous (from DNAPL, for example), depending on the rate of gas production. In these experiments, discontinuous FPG migration was seen because of the rate-limiting step for gas partitioning from the dissolved phase into the aqueous phase, and the fact that no new gaseous species were added to the sample once an experiment commenced.

3.3 Experimental Data Collected Towards a Revised SWCC

One experiment was run for each of the five grain sizes, and experimental data are shown in Figure 3.5. Here, each data point for a given experiment is representative of the saturation and fraction of

initial P_W prior unloading event in an experiment. This generated a soil-water saturation curve encompassing the effects of unsaturation with free phase gas formation.

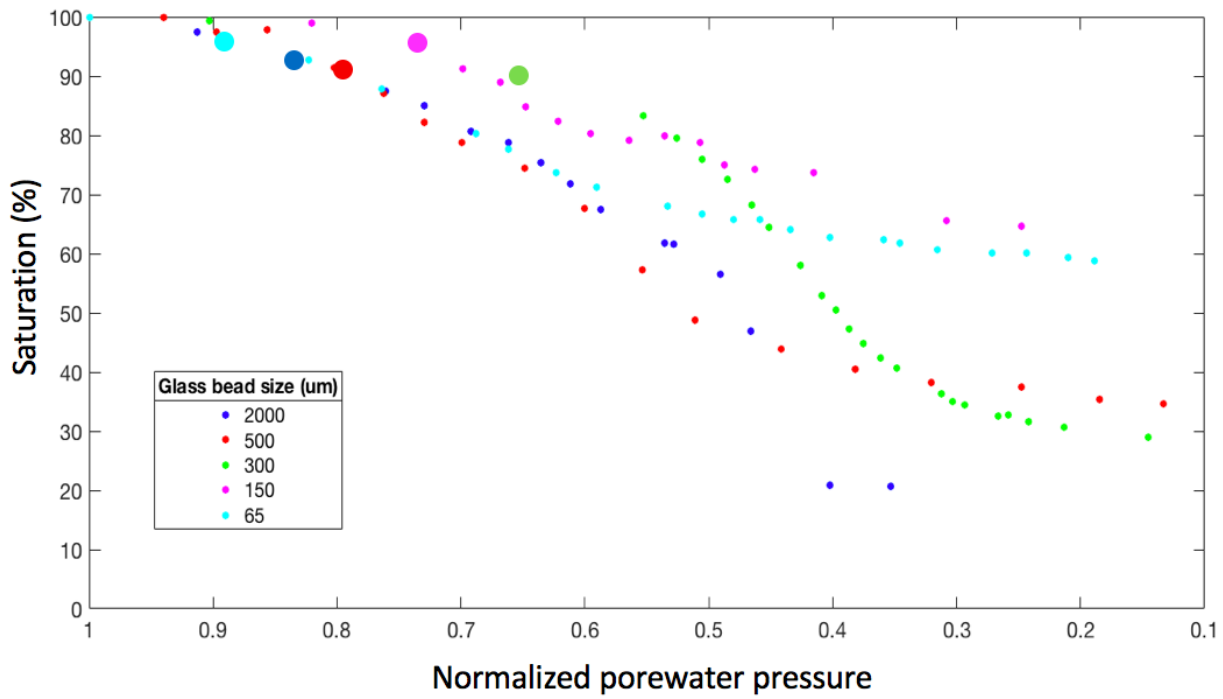

Figure 3.5: Experimental data of the unloading experiments (one experiment for each of the glass bead samples), comparing normalized porewater pressure (P_W) to saturation (%). Each porewater pressure measurement was divided by the initial P_W value for that experiment to get a fraction of the initial pressure (kPa/kPa), or normalized P_W value. Large data points indicate the point at which FPG invasion was visually observed for each experimental run.

Generally, this figure represents expected results when comparing P_w versus saturation for different grain (pore) sizes. All data curves show decreasing saturation with a loss in P_W. Initially, the rate of change in P_W is lower initially, then there is a more considerable loss in P_W as the slope gets steeper. The point at which FPG invasion occurred is highlighted on the figure (large data points), and tended to occur near an inflection point of the saturation and normalized P_W (Photographs in Appendix A3). FPG invasion may have happened sooner within pore of the beads

within the loading cell but could not be observed visually until invasion happened near the wall of the loading cell.

With continued desaturation, the slope approached zero towards end of the experiments. At local atmospheric pressure conditions, only the residual water is left in in the loading cell. There is an increasing trend in residual saturation with smaller grain sizes. This is attributed to smaller grains having a larger specific surface area [*Warrick*, 2002], and the surface beads adsorbing more water, and due to the higher energy demand required for removing water from the small pores. As such, beads with greater surface area for a given volume (i.e., volume of the loading cell) will have greater surface area thus a greater amount of residual, or adsorbed, water. The lack of consistent observation between residual saturation and grain size may be because of the relatively large size of the dielectric sensor probe with respect to the loading cell, resulting inaccurate bulk moisture content estimations.

3.3.1 On the Measurements of P_{CAP}

Based on existing knowledge of FPG body size and P_{CAP}, it was thought that smaller pores (glass beads) would have larger P_{CAP} values, and the difference between the P_W and P_{TDG} curves at equilibrium would provide an estimate of P_{CAP}, and the various experiments could then be compared to provide a relative estimate of pore size, FPG size, and capillary pressure.

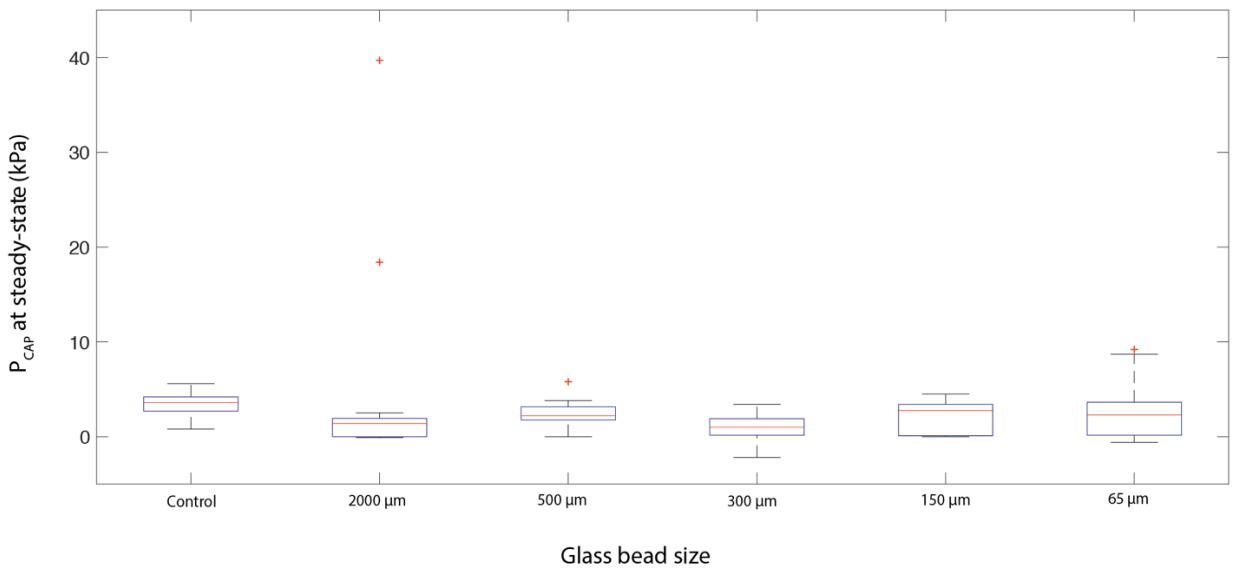

Figure 3.6: 'Box and whisker' plot showing the capillary pressures (P_{CAP}) at steady state for each experiment. Central red lines indicate the median values, the bottom and top of the box indicate the 25th and 75th percentiles, respectively, the whiskers indicate the extent of the observed data points, then then outliers are shown with + symbols.

However, there is no significant differences between any of the experiments from the various sizes of glass beads (Figure 3.6). This lack of significant difference could be due to the 3.5 mm drainage port located at the bottom of the loading cell in the bottom platen. The capillary pressure associated with this port could have dominated capillary pressure readings in the system. Because this port was consistent across all experiments, no significant difference was seen between the experiments.

No trends or significant differences were between P_{DROP}, P_{IN}, and P_{MIN}, saturation, and bead size in the experimental data (Appendix A3).

3.4 Towards a Free Phase Gas Characteristic Curve (FPG-CC)

The soil water characteristic curve commonly seen in unsaturated soil mechanics (Figure 1.4, for example), is revised here in a free phase gas characteristic curve (FPG-CC) to represent *in situ* free phase gas formation in initially saturated porous media at the pore-scale (Figure 3.7). It is assumed that the soil is initially fully saturated, and that no seed bubbles are initially present (thus no capillary pressure or FPG-water interface would be expected either. In the FPG-CC, P_W is assumed to be constant (i.e., assuming drained conditions), and P_{TDG} is greater than atmospheric pressure and is constantly increasing with *in situ* dissolved gas production. When P_{TDG} exceed P_W and P_{CAP} is when FPG bodies would form, causing a step function increase in PCAP (labelled as A in Figure 3.7).

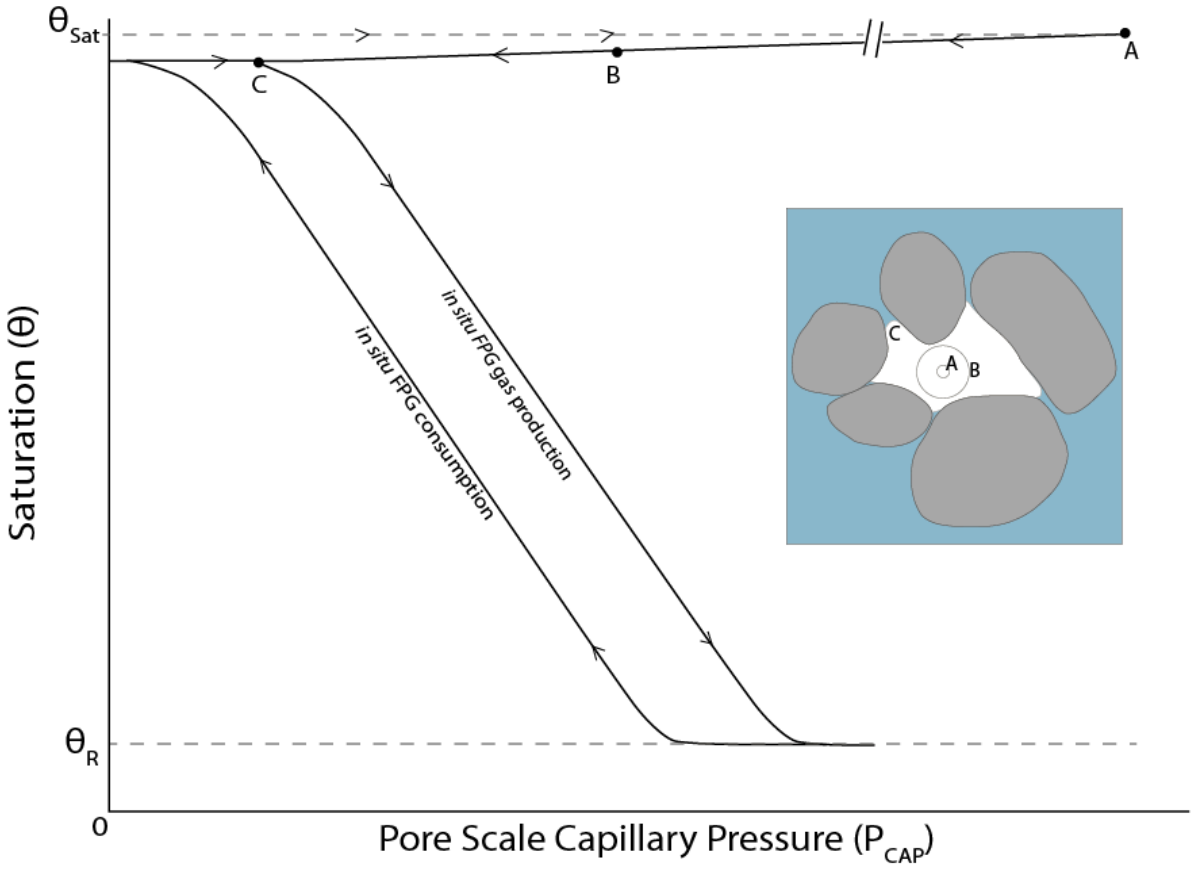

Figure 3.7: Pore scale free phase gas characteristic curve (psFPG-CC) depicting the relationship between capillary pressure and water content with *in situ* FPG production and consumption for a system where $P_{TDG} = P_W + P_{CAP}$. Starting at initially saturated conditions (illustration 1; i.e., no FPG present), FPG nucleates (A), increases in volume but is not limited by the pore throats (B), then invades multiple pores (C).

Under fully saturated conditions, a high nucleation energy is required for the first bubble to form [*Jones et al.*, 1999]. This high nucleation energy could require high P_{TDG} (relative to P_W), which, in the absence of a P_{CAP}, would be a state of disequilibrium. When the first exsolution happens, the small radii of the first microscopically small bubble seed(s) would be associated with a step-function increase in capillary pressure. The step-function increase in P_{CAP} would be short-lived, however, due to the relatively high value of P_{TDG} with respect to P_W, and this disequilibrium would result in partitioning of the 'excess' dissolved gas species into FPG, possibly until the water

content and P_{CAP} are in equilibrium with P_{TDG} and P_W, and located on the conventional SWCC curve familiar to us from soil-water characteristic curves. The time that the system might take to come to equilibrium would be analogous to the time between the unloading event and when P_W and P_{TDG} reached equilibrium, which is a function of diffusion of dissolved gas species in response to dissolved concentration gradients that occur when dissolved gas is partitioned in FPG at the onset of FPG formation.

With continued FPG production, FPG bodies will grow, and radii will increase, and capillary pressure decreases (see Section 3.2.2). Formation of FPG bodies and growth would push water out of the system (in a drained system), reducing saturation (labelled B in Figure 3.7). The inflection point in P_{CAP} (when it stops decreasing and starts to increase, C in Figure 3.7) occurs when FPG invades more than one pore, consequently decreasing the moisture content, with a decreased influence on P_{CAP}. It is important to note that more homogenous media (and thus more uniformly distributed pore sizes), the steeper the curve on a SWCC or psFPG-CC. Once the moisture content is below the inflection point, the capillary pressure is governed by the radius of the pores surrounding the larger FPG body that has expanded to invade increasingly large volumes of the porous media (Section 3.2.3). As FPG invasion and migration occurs, decreased saturation is associated with an increase in P_{CAP} because the FPG expansion is limited by the smallest pore throat radii in the invaded area, which is a function of pore draining patterns. In a system with different-sized pores, larger pores drain first, and small pores drain last. Upon draining, small pores retain their water, limited by the narrow pore throats. This factor also contributes to the increase in capillary pressure with decreased saturation. From the inflection point desaturation in an *in situ* FPG-production system proceeds as it does for SWCC. From this inflection point onwards, the

drainage process continues until FPG has driven out the porewater, leaving some residual saturation.

Although not experimentally evaluated in this thesis, if gas species were consumed *in situ* (i.e., by biogeochemical consumption), the system would re-saturate. Complete re-saturation (i.e., to 100% water saturation) would not be likely due to entrapped air being trapped in small pore spaces [*Pham et al.*, 2005].

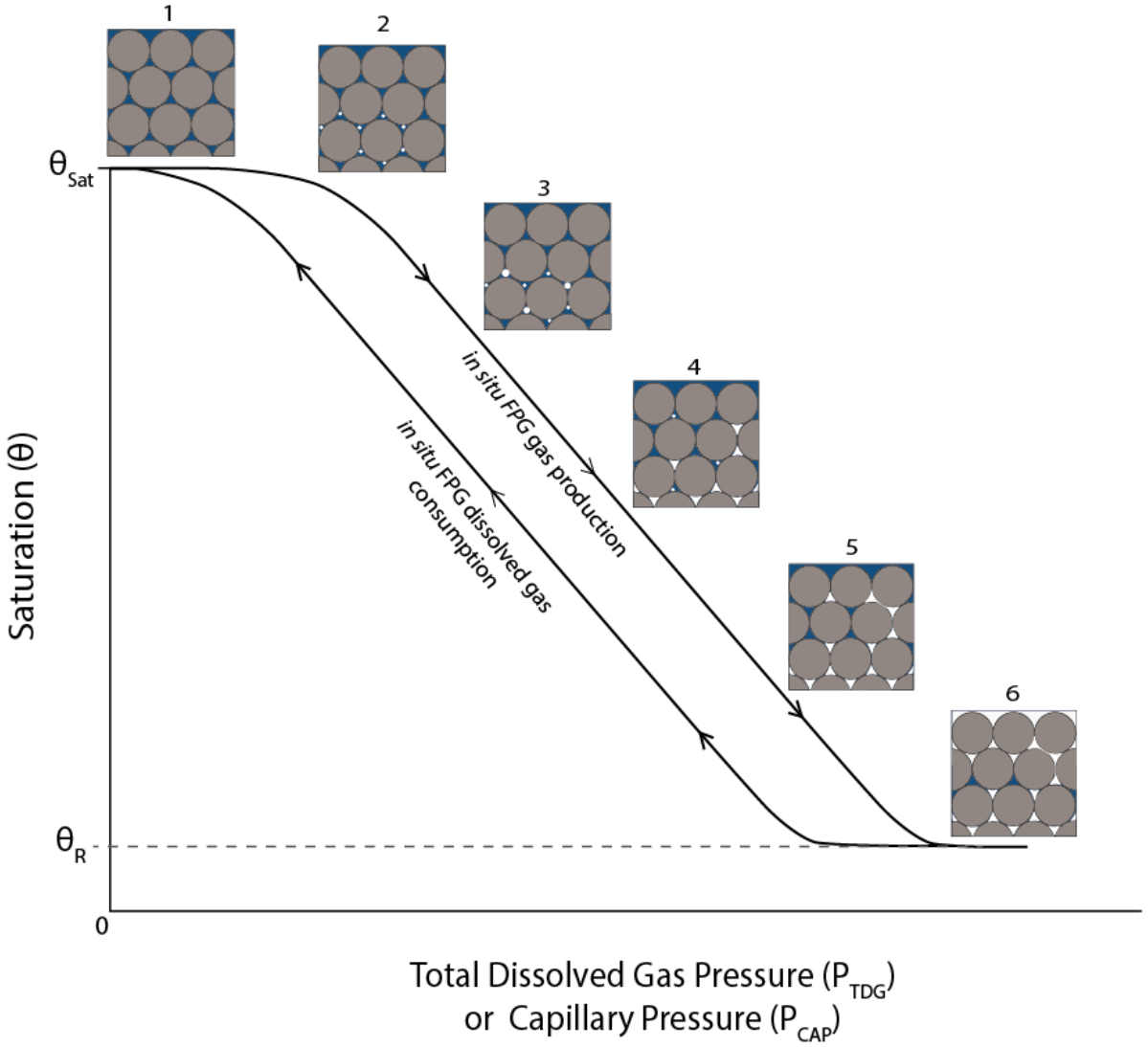

Figure 3.8: Free phase gas characteristic curve (FPG-CC) depicting the relationship between total dissolved gas pressure (P_{TDG}) or capillary pressure (P_{CAP}) and water content with *in situ* FPG production and consumption for a system where $P_{TDG} = P_W + P_{CAP}$. P_W is assumed to be constant. Starting at initially saturated conditions (i.e., no FPG present, schematic 1), FPG nucleates (2), expands within a pore (3), then invades multiple pores (4). Continued FPG production leads to FPG migration (5), ultimately forming an FPG cap (6). Re-saturation from FPG consumption shows hysteresis, and recovery to water contents/saturations less than initial saturation assuming complete collapse of FPG bodies from FPG consumption.

Now looking at the sample scale (i.e., not pore scale), the new FPG-CC would look similar to the existing SWCCs, as seen in Figure 3.8.. Additionally, it is important to note that in order for this FPG-CC to represent P_{TDG} or P_{CAP}, P_W would have to be constant. Starting with a fully saturated sample (1), FPG would nucleate (2), continue to expand (3) and invade multiple pores (4), migrate (5), and form an FPG cap (6). These processes occur just as they do in the psFPG-CC, however, there is no expected step-function increase, or subsequent decrease in capillary pressure following nucleation as was seen in the psFPG-CC. This is due to the difference in scales that these FPG-CC are representing.

Although we have assumed P_W is constant in the above discussion, changes in P_W would result in a three-dimensional FPG characteristic shape function (i.e. a family of FPG-CCs) beyond the scope of this work.

3.5 Conceptual Model for FPG Formation in Drained Condition

A conceptual model was developed to understand the changes in gas species partitioning and pressure distribution (P_{TDG}, P_{CAP} and P_{BUOY}) as a single FPG body forms, and increases in volume with time due to *in situ* dissolved gas production. Typically in soil mechanics, experimental conditions are either to considered as ‘drained’ or ‘undrained’, depending on whether air and water can drain after the application or removal of a total stress increment [*Fredlund and Rahardjo*, 1993]. In the model developed in this section, total volume of the system remains constant, but volume of water and FPG change throughout the modelled time.

Two numerical models using synthetic data reproduce the conceptual relationships proposed and are found in Appendix A4. The first model neglected compressibility of matrix, water, and FPG, and the second model incorporated compressibility of water but assumes compressibility of FPG and matrix are negligible.

In Figure 3.9, it is assumed that: i) no microscopic seed bubbles are present, ii) only one FPG body is forming, iii) it forms in 'drained' conditions (i.e., constant P_W), and any increase in FPG volume results in immediate drainage, iv) the rate of *in situ* dissolved gas production is constant, and v) that the compressibility of matrix, water, and dissolved and free gas phases are negligible, and vi) the system is at equilibrium with respect to Henry's Law (i.e., diffusion happens quickly and dissolved gas concentrations are constant everyone at any given time). In panel i, *in situ* gas production is causing an increase in the dissolved gas concentration. This in turn causes an increase in P_{TDG}, and because P_{TDG} has not exceeded P_W, no FPG is present. The transition to (ii) occurs when P_{TDG} exceeds P_W. At this point, the single bubble in the system has formed. This conceptual model assumes no pre-existing FPG bodies are in the system. It is likely that nucleation would occur at a narrow interface or on an impurity, such as a surfactant [*Jones et al.*, 1999].

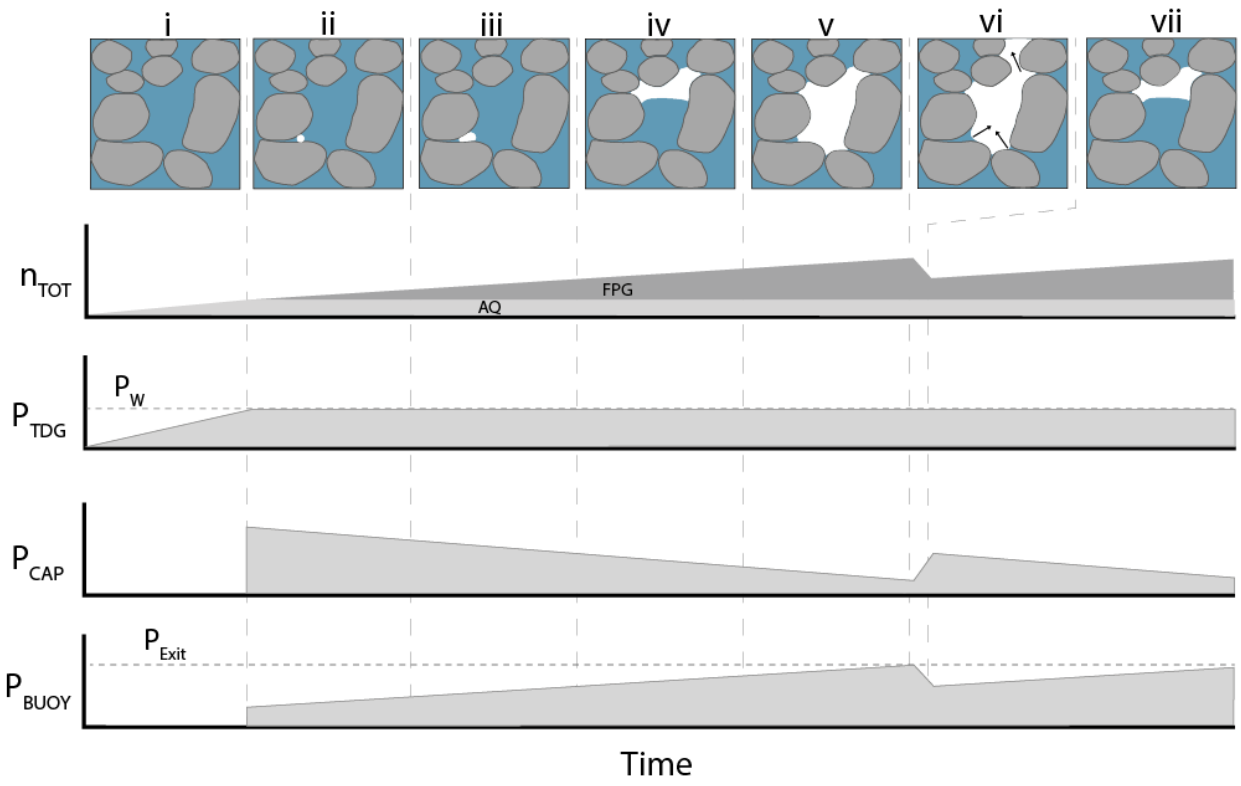

Figure 3.9: Conceptual model of a bubble nucleating, growing, and migrating out of the area of interest, from *in situ* free phase gas production. Total number of moles of gaseous species (n_{TOT}), total dissolved gas pressure (P_{TDG}), capillary pressure (P_{CAP}), and buoyancy pressure (P_{BUOY}) are illustrated. Here, P_W is assumed to be constant, and there is a constant rate of *in situ* gas production.

The presence of FPG in equilibrium with P_{TDG} indicates that the water is saturated with respect to dissolved gas (or, that P_{TDG} is equal to the sum of P_{CAP} and P_W). Any subsequent *in situ* dissolved gas production would increase the volume of FPG. Since P_W is constant (i.e. the systems 'drains' as FPG is formed), P_{TDG} would plateau at this point at its maximum value at this point. Although the dissolved gas concentration does not increase, given P_W remains constant because any FPG volume growth is causing water to exit the system (i.e., drained system). The incipient bubble would have a small radius, and as such, there would be a commensurately large, and step-function,

increase in P_{CAP} due to rapid formation of FPG bodies [*Ryan et al.*, 2015]. Also, the formation of the initial bubble would associate with a step-function increase in buoyancy pressure, P_{BUOY}. As the bubble increases in size with continued gas species production (panels iii through v), n_{FPG}, and P_{BUOY} steadily increase as P_{CAP} decreases. Once P_{BUOY} exceeds the pore exit pressure of the largest pore throat (i.e., smallest P_E; Figure 3.4), the FPG body will exit through that pore throat. Free phase gas migration occurs until the remaining FPG body no longer has the FPG height to maintain a P_{BUOY} that exceeds P_E. At this point, what is remaining of the single bubble will be 're-trapped' until enough dissolved gas is generated *in situ* to cause sufficient mass diffusion into the FPG body to increase the FPG body's P_{BUOY} to be sufficiently large to overcome the P_E threshold again.

4 CONCLUSION

Free phase gas forms when a dissolved gas becomes supersaturated in the water due to a reduction in P_W and/or a P_{TDG} increase (i.e., by biogeochemical gas production) beyond the bubbling pressure. In the experiments conducted here, the supersaturation of gas in water was invoked by a porewater pressure reduction (i.e., P_W was reduced below P_{TDG} values). This resulted in the partitioning of dissolved gas phase into free-phase gas after each unloading event, with a subsequent "rebound" to equilibrium P_W. The time required to reach equilibrium represented the time required for dissolved gas transport to occur by diffusion until the Henry's coefficient was satisfied, and/or P_{CAP} was minimized.

A conceptual soil-water characteristic curve (SWCC) was adapted to represent desaturation and re-saturation of an initially saturated media (i.e., formation and/or consumption of FPG in a previously saturated media) by *in situ* dissolved gas formation or consumption. In this revised SWCC, called a free phase gas characterization curve (FPG-CC) here, water desaturation is initiated when in situ dissolved gas production causes P_{TDG} to exceeds the bubbling pressure sufficiently to cause FPG exsolution.

Although SWCC are only ever considered for a constant P_{TDG} (i.e. atmospheric pressure), the variation of both P_W and P_{TDG} in the subsurface means that a complete FPG-CC is a three-dimensional surface, or a 'family' of FPG-CCs.

At initial conditions (i.e., assuming complete saturation with no macroscopic bubbles present), there is no capillarity in the system as there is no FPG-water interface. The nucleation of the first bubble results requires nucleation energy, which may result in P_{TDG} disequilibrium, where P_{TDG} values may need to exceed P_{BUB} values, before the first bubble is formed. The first bubble will initially be small, with commensurately high P_{CAP}, and partitioning is to satisfy Henry's Law. As dissolved gases partition in the FPG during FPG body formation, the dissolved concentrations decrease and concentration gradients occur, resulting in diffusion of dissolved gas according to Fick's Law. Dissolved gas diffuses towards, and then partitions into, the FPG body until an equilibrium is reached where Henry's Law, Fick's Law, and capillary pressure are satisfied. As the number of moles in FPG form increase, the FPG body radius increases, and P_{CAP} decreases. In the lab experiments conducted, this transient process took about two hours, then a new equilibrium was reached. Continued partitioning of gas causes FPG to invade multiple pores. Here, capillary pressure is limited by the pore of the smallest throat. When the FPG body is large enough for its buoyancy to exceed the pore throat exit pressure, then FPG migration occurs.

FPG body dimensions are limited by pore or pore throat size. When this occurs, P_{CAP} values increase due to the FPG body being squeezed through small pore throats. The increase in P_{CAP} with desaturation is a reflection of to the preferential pattern of large pores draining first, leaving air-water interfaces in progressively smaller pore spaces. If *in situ* dissolved gas consumption results in re-saturation, hysteresis effects would be expected as smaller pores would fill first. Additionally, re-saturation by FPG consumption would likely not result in complete re-saturation due to the energetically unfavourable conditions of collapsing small bubbles. If, a small portion of the sample

would remain unsaturated as a result of FPG entrapment. These small FPG bodies act as the nucleation points for subsequent unloading events.

Important differences between the FPG-CC and the SWCC include: i) incorporation of an additional variable, P_{TDG}, into the conceptual model (which is constant and equal to P_{ATM} in the vadose zone), ii) the need to present moisture content or saturation as a function of P_{CAP} (as opposed to P_W), or alternatively P_{TDG}, and iii) initial capillary pressures when the first FPG body is formed in initially truly saturated sediment.

Capillary pressure (P_{CAP}; equal to the difference between P_{TDG} and P_W) could not be measured for the air-water interface of bubbles due to equipment limitations in the uniaxial apparatus. Large pore throats in the drainage system, in addition to thick-walled silicon tubing largely governed P_{CAP} determination in this experimental setup.

Higher water saturation values were retained in finer grained media at any given pore pressure due to the competing influence of: i) earlier invasion due to smaller pore spaces, and ii) higher P_E required for FPG migration in fine-grained media. At atmospheric pressures, higher VWC retained in finer grained media was due to the increased specific surface area of smaller grains adsorbing more water.

The relationship between P_{CAP} and saturation in the FPG-CC can contribute to a better understand of the pore-scale processes occurring in areas with naturally-occurring FPG in formerly saturated zones. A more robust understanding of P_{CAP} and saturation on a pore-scale can be used in context

to better understand field scales where FPG has been implicated (e.g., overpressurized units, remote triggering of earthquakes, marine and tidally-influenced settings, and dry coal beds). Overall, this work contributes to a better understanding of FPG formation and expansion initially saturated sediment.

5 FUTURE WORK

Visualizing the formation and expansion of FPG would be advantageous in providing better insight in FPG relationships in pore spaces. Visualization can be done with X-ray tomography and CT scans [*Wildenschild and Sheppard*, 2013]. Additionally, in order to image the partitioning of gas in FPG and water, other laboratory-based techniques have been developed to image using specially-designed flow-through chambers [*Van De Ven and Mumford*, 2018].

In order to maintain total stress in the system, these experiments can be repeated with changed temperature instead of minute release of gas and water. The change in temperature will lead to a change in solubility of the gas, causing exsolution and expansion. This can be done in stages to repeat the experiment and can be done in the reverse order to create figures show hysteresis effects. Hysteresis effects are seen in other soil-water characteristic curves show that path of saturation and desaturation are not identical. This is expected with FPG expansion and collapse too, as small FPG bodies form first and drain last.

Additionally, these experiments can be repeated in triaxial apparatus. This was, reductions in the magnitude of principle stress reducing pore pressure without losing liquid. This will also result in gas exsolution. Moreover, triaxial apparatuses are equipped with P and S wave platens to detect FPG nucleation. A further step in the triaxial apparatus could be to move from glass beads to sandstone cores to examine the effects in rock.

The gas in the water can be generated *in situ* using microorganisms. Under the right conditions, bacteria can produce methane or nitrogen gas which will saturate water. Past the saturation point, FPG will exsolve. This can be continued to the point of fracturing of a sandstone and better represent natural processes in the subsurface and provide insight as to whether or not FPG production can cause rock to fracture.

REFERENCES

Aeschbach-Hertig, W., F. Peeters, U. Beyerie, and R. Kipfer (1999), Interpretation of dissolved atmospheric noble gases, *Water Resour. Res.*, *35*(9), 2779–2792.

Aizawa, K. et al. (2016), Gas pathways and remotely triggered earthquakes beneath Mount Fuji, Japan, *Geology*, doi:10.1130/G37313.1.

Alberta Agriculture and Forestry (2006), *Dissolved gases in groundwater*, Edmonton, Alberta.

Amaratunga, A., and J. L. H. Grozic (2009), On the undrained unloading behaviour of gassy sands, *Can. Geotech. J.*, *46*(11), 1267–1276, doi:10.1139/T09-056.

Amos, R. T., K. U. Mayer, B. A. Bekins, G. N. Delin, and R. L. Williams (2005), Use of dissolved and vapor-phase gases to investigate methanogenic degradation of petroleum hydrocarbon contamination in the subsurface, *Water Resour. Res.*, *41*(2), 1–16, doi:10.1029/2004wr003433.

ASTM International (2008), ASTM D6836: Standard Test Methods for Determination of the Soil Water Chararcteristic Curve for Desorption Using Hanging Column, Pressure Extractor, Chilled Mirror Hygrometer, or Centrifuge, *ASTM Int.*, (D6836-02), 1–22, doi:10.1520/D6836-02R08E02.characteristic.

Azam, S., M. Ito, and F. Khan (2013), Influence of cracks on soil water characteristic curve, *Adv. Unsaturated Soils- Caicedo al.*, 217–220.

Bastian, P., O. Wirth, L. Wang, and G. Voneiff (2005), Assessment and Development of the Dry Horseshoe Canyon CBM Play in Canada, in *Proceedings of SPE Annual Technical Conference and Exhibition*, Dallas, Texas.

Bauget, F., and R. Lenormand (2002), Mechanisms of bubble formation by pressure decline in porous media: A critical review, in *SPE Annual Technical Conference and Exhibition*, pp.

1–10, San Antonio, Texas.

Beaton, A. (2003), *Production Potential of Coalbed Methane Resources in Alberta*.

Bicalho, K., D. Znidaric, and H.-Y. Ko (2005), Measurement of soil-water characteristic curves of quasi-saturated soils, in *Proceedings of 16th International Conference on Soil Mechanics and Geotechnical Engineering*, pp. 1019–1022.

Bora, R., and B. B. Maini (1997), BoraMainiChakma_SPE1997.pdf, in *SPE International Thermal Operations and Heavy Oil Symposium*, Bakersfield, California.

Boudreau, B. P. (2012), The physics of bubbles in surficial, soft, cohesive sediments, *Mar. Pet. Geol.*, *38*(1), 1–18, doi:10.1016/j.marpetgeo.2012.07.002.

Bowers, G. L. (2002), Detecting high overpressure, *Lead. Edge*, *21*(2), 174–177, doi:10.1190/1.1452608.

Brady, J. E., and F. Senese (2009), *Chemistry: matter and its changes*, Fifth., edited by S. Johnson, John Wiley and Sons, Inc.

Cadogan, S. P., G. C. Maitland, and J. P. M. Trusler (2014), Diffusion coefficients of CO2 and N2 in water at temperatures between 298.15 K and 423.15 K at pressures up to 45 MPa, *J. Chem. Eng. Data*, *59*(2), 519–525, doi:10.1021/je401008s.

de Chalendar, J. A., C. Garing, and S. M. Benson (2018), Pore-scale modelling of Ostwald ripening, *J. Fluid Mech.*, *835*, 363–392, doi:10.1017/jfm.2017.720.

de Chalendar, J. (2016), Impact of Ostwald ripening on residually trapped carbon dioxide, Stanford University.

Chen, X., and L. Slater (2015), Gas bubble transport and emissions for shallow peat from a northern peatland: The role of pressure changes and peat structure, *Water Resour. Res.*, (51), 151–168, doi:10.1002/2014WR016852.Received.

Christian, H. A., D. J. Woeller, P. K. Robertson, and R. C. Courtney (1997), Site investigations to evaluate flow liquefaction slides at Sand Heads, Fraser River delta, *Can. Geotech. J.*, *34*(3), 384–397, doi:10.1139/t97-004.

Cook, P. G., and J. K. Bohlke (2000), Determining timescales for groundwater flow and solute transport in, in *Environmental Tracers in Subsurface Hydrology*, pp. 1–30.

Crews, J. B., and C. A. Cooper (2012), Bubble nucleation in groundwater triggered by seismic stimulation: A laboratory study, in *46th U.S. Rock Mechanics/Geomechanics Symposium*, Chicago, Illinois.

Crews, J. B., and C. A. Cooper (2014), Experimental evidence for seismically initiated gas bubble nucleation and growth in groundwater as a mechanism for coseismic borehole water level rise and remotely triggered seismicity, *J. Geophys. Res. Solid Earth*, *119*, 7079–7091, doi:10.1002/2014JB011398.Received.

D'Aoust, B. G., and M. J. R. Clark (1980), Transactions of the American Fisheries Society Analysis of Supersaturated Air in Natural Waters and Reservoirs Analysis of Supersaturated, *ransactions Am. Fish. Soc.*, *109*(1980), 708–724, doi:10.1577/1548-8659(1980)109<708.

Decagon Devices Inc. (2016), *EC-5 Soil Moisture Sensor Operator's Manual*.

Dusseault, M. B. (1979), Undrained volume and stress change behavior of unsaturated very dense sand, *Can. Geotech. J.*, *16*(4), 627–640, doi:10.1139/t10-0.

Esrig, M. I., and R. C. Kirby (1977), Implications of gas content for predicting the stability of submarine slopes, *Mar. Geotechnol.*, *2*(1–4), 81–100, doi:10.1080/10641197709379771.

Evans, R. (2017), Towards accurate in situ dissolved gas concentration estimations in gas-charged groundwater using field measured total dissolved gas pressure (PTDG), University

of Calgary.

Fox, A. D., and M. Soltanzadeh (2015), A Regional Geomechanical Study of the Duvernay Formation in, *GeoConvention*, 1–4.

Fredlund, D. G. (2017), Role of soil-water characteristic curve in unsaturated soil mechanics, in *Proceedings of the 19th International Conference on Soil Mechanics and Geotechnical Engineering*, Seoul, South Korea.

Fredlund, D. G., and H. Rahardjo (1993), *Soil Mechanics for Unsaturated Soils*, John Wiley and Sons, New York, NY.

Fredlund, D. G., and A. Xing (1994), Equations for the soil-water characteristic ' curve ', *Can. Geotech. J.*, *31*(4), 521–532, doi:10.1139/t94-120.

Fredlund, D. G., D. Sheng, and J. Zhao (2011), Estimation of soil suction from the soil-water characteristic curve, *Can. Geotech. J.*, *48*(2), 186–198, doi:10.1139/T10-060.

Fredlund, D. G., H. Rahardjo, and M. D. Fredlund (2018), Understanding the Family of Soil-Water Characteristic Curves, in *GeoEdmonton*, pp. 1–7.

Furbish, D. J. (1997), *Fluid physics in geology*, Oxford University Press, New York, NY.

Haththotuwa, C. K., and J. L. H. Grozic (2011), Effect of fines content on instability behaviour of loose silt-sands containing gas bubbles, in *2011 Pan-Am CGS Geotechnical Conference*, pp. 1–8.

Heaton, T. H. E. (1981), Dissolved Gases: Some applications to groundwater research, in *Transactions of the Geological Society of South Africa*, pp. 91–87.

Hillel, D. (2004), *Introduction to Environmental Soil Physics*, Elsevier Science (USA).

Hoch, O. (2005), The Dry Coal Anomaly — The Horseshoe Canyon Formation of Alberta, Canada, in *2005 SPE Annual Technical Conference and Exhibition*, vol. 1, pp. 1–14, Dallas,

Texas.

Hong, W.-T., Y.-S. Jung, S. Kang, and J.-S. Lee (2016), Estimation of Soil-Water Characteristic Curves in Multiple-Cycles Using Membrane and TDR System Won-Taek, *Materials (Basel).*, *9*, 1–15.

Ingebritsen, S. E., W. E. Sanford, and C. E. Neuzil (2011), *Groundwater in geologic processes*, Second Edi., Cambridge University Press.

Jang, J., and J. C. Santamarina (2014), Evolution of gas saturation and relative permeability during gas production from hydrate-bearing sediments: Gas invasion vs. gas nucleation, *J. Geophys. Res. Solid Earth Res.*, *119*, 116–126, doi:10.1002/2015JB012140.Received.

Jones, S. F., G. M. Evans, and K. P. Galvin (1999), Bubble nucleation from gas cavities - A review, *Adv. Colloid Interface Sci.*, *80*(1), 27–50, doi:10.1016/S0001-8686(98)00074-8.

Jury, W. A., and R. Horton (2004), *Soil physics*, Sixth Edit., John Wiley and Sons, Inc.

Ladd, B. S., and M. C. Ryan (2016), Can CO2 trigger a thermal geyser eruption?, *Geology*, *44*(4), 307–310, doi:10.1130/G37588.1.

Li, X., J. H. Li, and L. M. Zhang (2014), Predicting bimodal soil-water characteristic curves and permeability functions using physically based parameters, *Comput. Geotech.*, *57*, 85–96, doi:10.1016/j.compgeo.2014.01.004.

Lichstein, H. C., and M. H. Soule (1943), 1. The Action of Sodium Azide on Microbic Growth, *Stud. Eff. sodium azide microbic growth Respir.*, 1–10.

Mahabadi, N., S. Dai, Y. Seol, T. S. Yun, and J. Jang (2016), The water retention curve and relative permeability for gas production from hydrate-bearing sediments: pore-network model simulation Nariman, *Geochemistry Geophys. Geosystems*, *17*, 3099–3110, doi:10.1002/2015GC006060.Received.

Manning, A. H., D. K. Solomon, and A. L. Sheldon (2003), Applications of a total gas pressure probe in ground water studies, *Groundwater*, *41*(4), 440–448.

Miller, S. A., C. Collettini, L. Chiaraluce, M. Cocco, M. Barchi, and B. J. P. Kaus (2004), Aftershocks driven by a high-pressure CO2 source at depth, *Nature*, *427*(6976), 724–727, doi:doi: 10.1038/nature02251.

Mumford, K. G., S. E. Dickson, and J. E. Smith (2009), Slow gas expansion in saturated natural porous media by gas injection and partitioning with non-aqueous phase liquids, *Adv. Water Resour.*, *32*, 29–40.

Naber, A., C. Liu, and J. J. Feng (2008), The nucleation and growth of gas bubbles in a Newtonian fluid: an energetic variational phase field approach, *Contemp. Math.*, *466*(50390095), 95–120, doi:10.1090/conm/466.

Nejad, K. S., A. Danesh, and P. Engineering (2005), Visual Investigation of Oil Depressuristion in Pores with Different Wettability Characteristics and Saturation Histories, in *SPE Europec/EAGE Annual Conference*, Madrid, Spain.

Osborne, M. J., and R. E. Swarbrick (1997), Mechanisms for Generating Overpressue in Sedimentary Basins - a Reevaluation, *Gener. Overpressure*, *6*(6), 1023–1041.

Pankow, J. F., and J. A. Cherry (1996), *Dense Chlorinated Solvents and other DNAPLs in Groundwater*, Waterloo Press, Guelph, Ontario.

Pham, H. Q., D. G. Fredlund, and S. L. Barbour (2003), A practical hysteresis model for the soil–water characteristic curve for soils with negligible volume change, *Géotechnique*, *53*(2), 293–298, doi:10.1680/geot.2003.53.2.293.

Pham, H. Q., D. G. Fredlund, and S. L. Barbour (2005), A study of hysteresis models for soil-water characteristic curves, *Can. Geotech. J.*, *42*(6), 1548–1568, doi:10.1139/t05-071.

Rahimi, A., H. Rahardjo, and E. C. Leong (2015a), Effect of range of soil-water characteristic curve measurements on estimation of permeability function, *Eng. Geol.*, *185*, 96–104, doi:10.1016/j.enggeo.2014.11.017.

Rahimi, A., H. Rahardjo, and E. C. Leong (2015b), Effects of soil-water characteristic curve and relative permeability equations on estimation of unsaturated permeability function, *Soils Found.*, *55*(6), 1400–1411, doi:10.1016/j.sandf.2015.10.006.

Ramdhan, A. M., and N. R. Goulty (2011), Overpressure and mudrock compaction in the Lower Kutai Basin, Indonesia: A radical reappraisal, *Am. Assoc. Pet. Geol. Bull.*, *95*(10), 1725–1744, doi:10.1306/02221110094.

Roy, J. W., and M. C. Ryan (2010), In-Well Degassing Issues for Measurements of Dissolved Gases in Groundwater, *Ground Water*, *48*(6), 869–877, doi:10.1111/j.1745-6584.2010.00703.x.

Roy, J. W., and M. C. Ryan (2013), Effects of unconventional gas development on groundwater: A call for total dissolved gas pressure field measurements, *Groundwater*, *51*(4), 480–482, doi:10.1111/gwat.12065.

Ryan, M. C. (2017), Groundwater, bubbles, and energy: the 2017 Farvolden Lecture,

Ryan, M. C., K. T. B. MacQuarrie, J. Harman, and J. McLellan (2000), Field and modeling evidence for a "stagnant flow" zone in the upper meter of sandy phreatic aquifers, *J. Hydrol.*, *233*(1–4), 223–240, doi:10.1016/S0022-1694(00)00236-5.

Ryan, M. C., J. W. Roy, and D. J. Heagle (2015), Dissolved gas 'concentrations' or 'concentration estimates' – A comment on "Origin, distribution and hydrogeochemical controls on methane occurrences in shallow aquifers, southwestern Ontario, Canada" by Jennifer C. McIntosh, Stephen E. Grasby, Stewart M., *Appl. Geochemistry*, *63*, 218–221,

doi:http://dx.doi.org/10.1016/j.apgeochem.2015.08.015.

Sobkowicz, J. C., and N. R. Morgenstern (1984), The undrained equilibrium behaviour of gassy sediments, *Can. Geotech. J.*, *21*, 439–448.

Stanley, F. K. T., S. Zarezadeh, C. D. Dumais, K. Dumais, R. MacQueen, F. Clement, A. A. Goodarzi, and Abstract (2017), Comprehensive survey of household radon gas levels and risk factors in southern Alberta, *C. OPEN*, *5*(1), E255–E264.

Vanapalli, S. K., D. G. Fredlund, D. E. Pufahl, and A. W. Clifton (1996), Model for the prediction of shear strength with respect to soil suction, *Can. Geotech. J.*, *33*, 379–392.

Van De Ven, C. J. C., and K. G. Mumford (2018), Visualization of gas dissolution following upward gas migration in porous media: Technique and implications for stray gas, *Adv. Water Resour.*, *115*, 33–43, doi:10.1016/j.advwatres.2018.02.015.

Wang, M., L. Kong, and M. Zang (2015), Effects of sample dimensions and shapes on measuring soil-water characteristic curves using pressure plate, *J. Rock Mech. Geotech. Eng.*, *7*(4), 463–468, doi:10.1016/j.jrmge.2015.01.002.

Warrick, A. W. (2002), *Soil Physics Companion*, CRC Press LLC, Boca Raton, Florida.

Wheeler, S. J. (1988), A conceptual model for soils containing large gas bubbles, *Géotechnique*, *38*, 389–397.

Wildenschild, D., and A. P. Sheppard (2013), X-ray imaging and analysis techniques for quantifying pore-scale structure and processes in subsurface porous medium systems Dorthe, *Adv. Water Resour. J.*, *51*, 217–246, doi:10.1016/j.advwatres.2012.07.018.

Wilson, R. D., and D. M. Mackay (1996), SF6 as a conservative tracer in saturated media with high intragranular porosity or high organic carbon content, *Ground Water*, *34*(2), 241–249.

Wong, R. C. K., and B. B. Maini (2007), Gas bubble growth in heavy oil-filled sand packs under

undrained unloading, *J. Pet. Sci. Eng.*, *55*(3–4), 259–270, doi:10.1016/j.petrol.2006.08.006.

Zhai, Q., and H. Rahardjo (2012), Determination of soil-water characteristic curve variables, *Comput. Geotech.*, *42*, 37–43, doi:10.1016/j.compgeo.2011.11.010.

Zhai, Q., and H. Rahardjo (2015), Estimation of permeability function from the soil-water characteristic curve, *Eng. Geol.*, *199*, 148–156, doi:10.1016/j.enggeo.2015.11.001.

Zhang, F., Z. Wang, H. Zhong, Y. Song, W. Liu, and C. Wei (2016), Origin of abnormal high pressure and its relationship with hydrocarbon accumulation in the Dina 2 Gas Field, Kuqa Depression, *Pet. Res.*, *1*, 93–102.

APPENDIX A1: EXPERIMENTAL DATA FROM EACH GRAIN SIZE

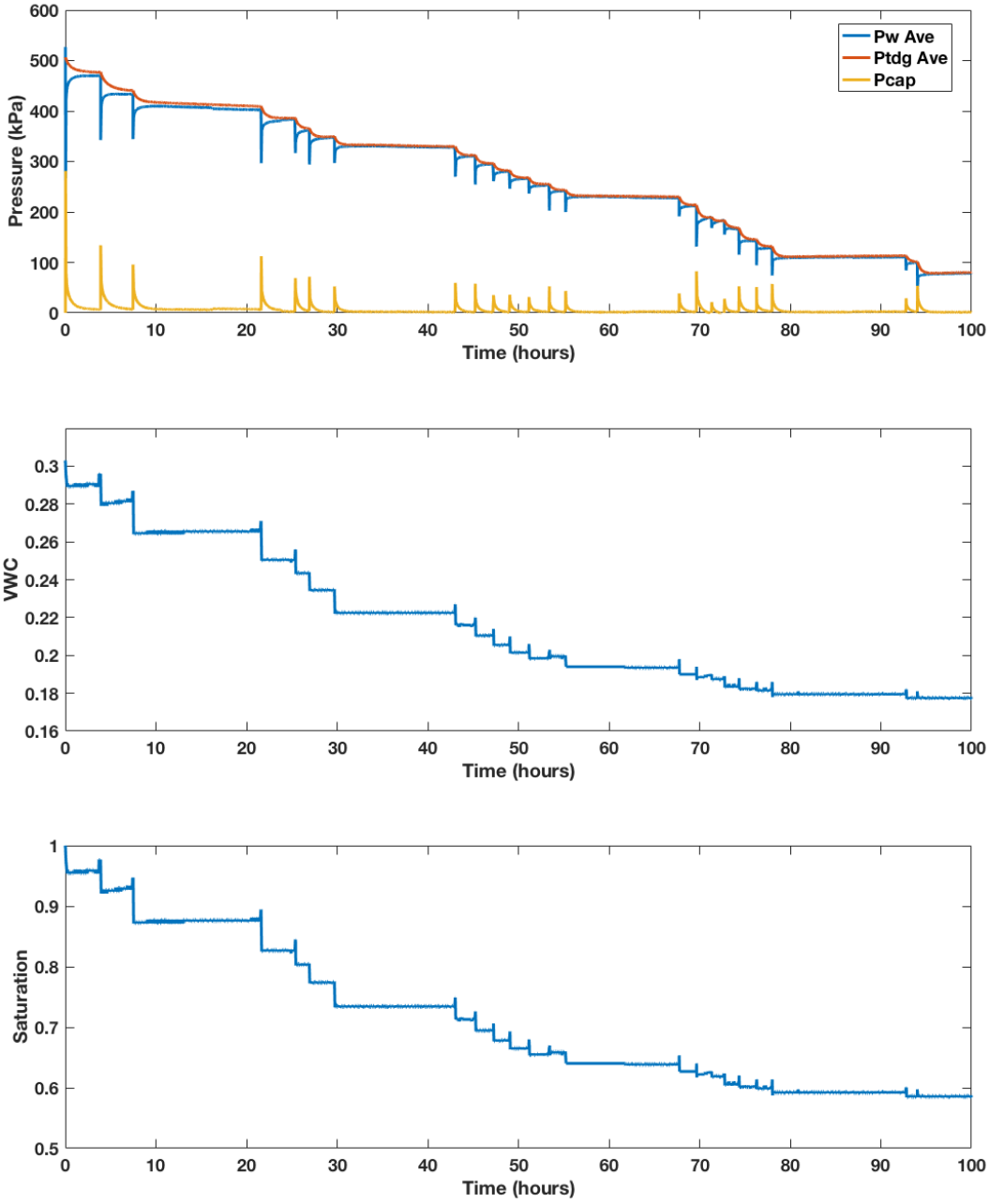

Figure A1.1: Data from experiment using 65 μm glass beads. Top figure shows P_W (blue), P_{TDG} (red), and P_{CAP} (orange). Middle figure shows Volumetric water content (VWC), and bottom figure is saturation when VWC data are divided by VWC value with maximum water saturation.

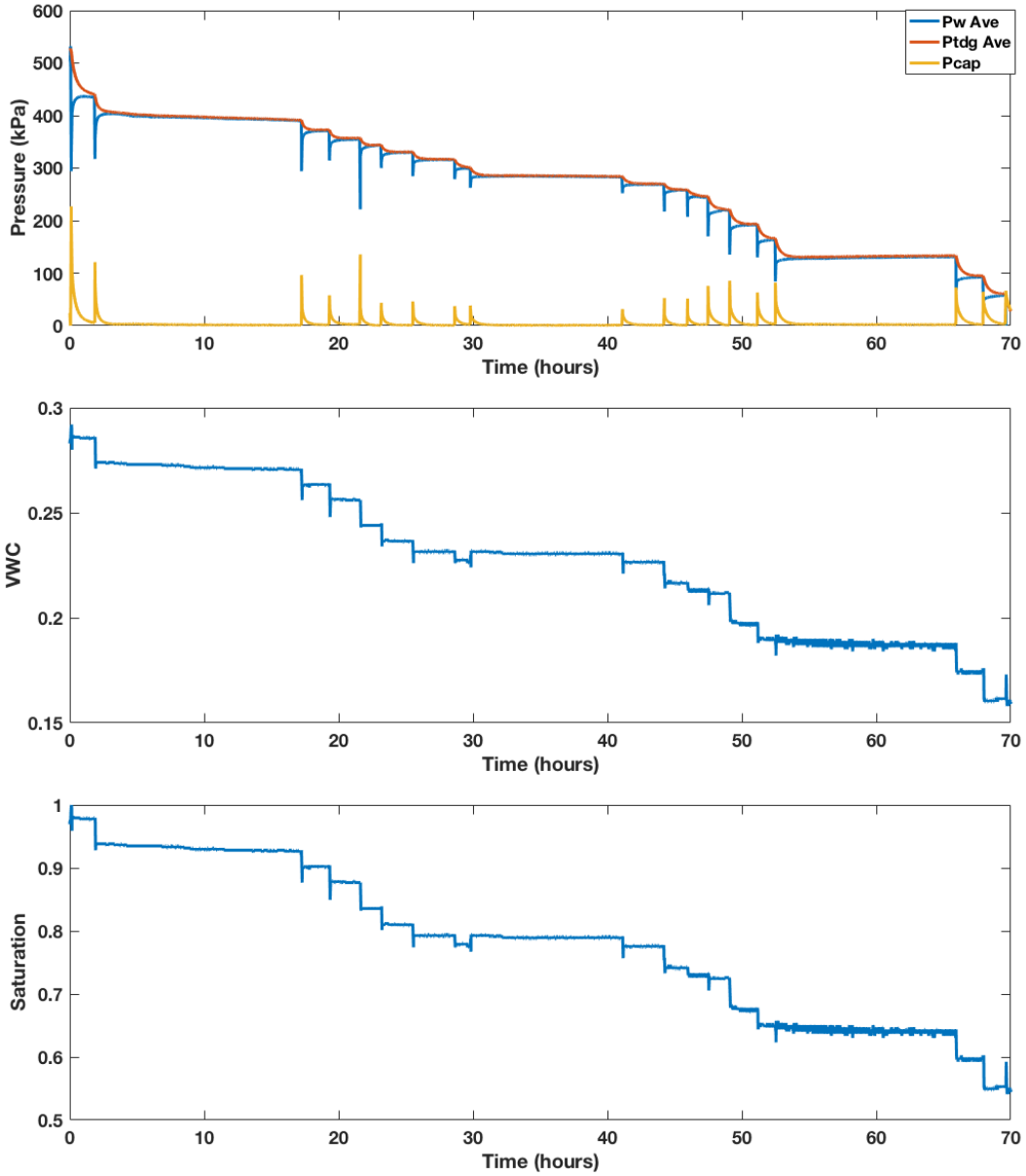

Figure A1.2: Data from experiment using 150 μm glass beads. Top figure shows P_W (blue), P_{TDG} (red), and P_{CAP} (orange). Middle figure shows Volumetric water content (VWC), and bottom figure is saturation when VWC data are divided by VWC value with maximum water saturation.

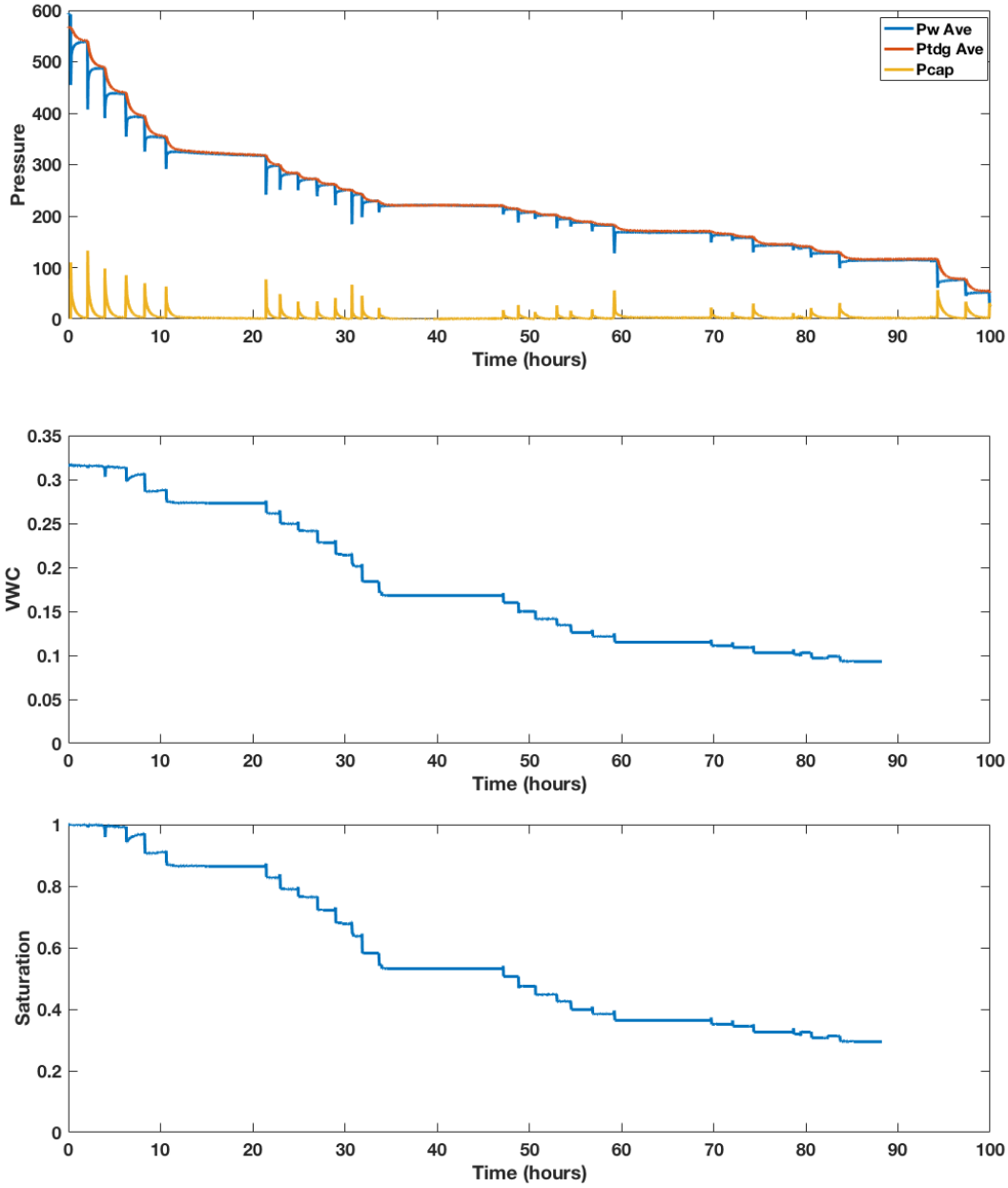

Figure A1.3: Data from experiment using 300 μm glass beads. Top figure shows P_W (blue), P_{TDG} (red), and P_{CAP} (orange). Middle figure shows Volumetric water content (VWC), and bottom figure is saturation when VWC data are divided by VWC value with maximum water saturation.

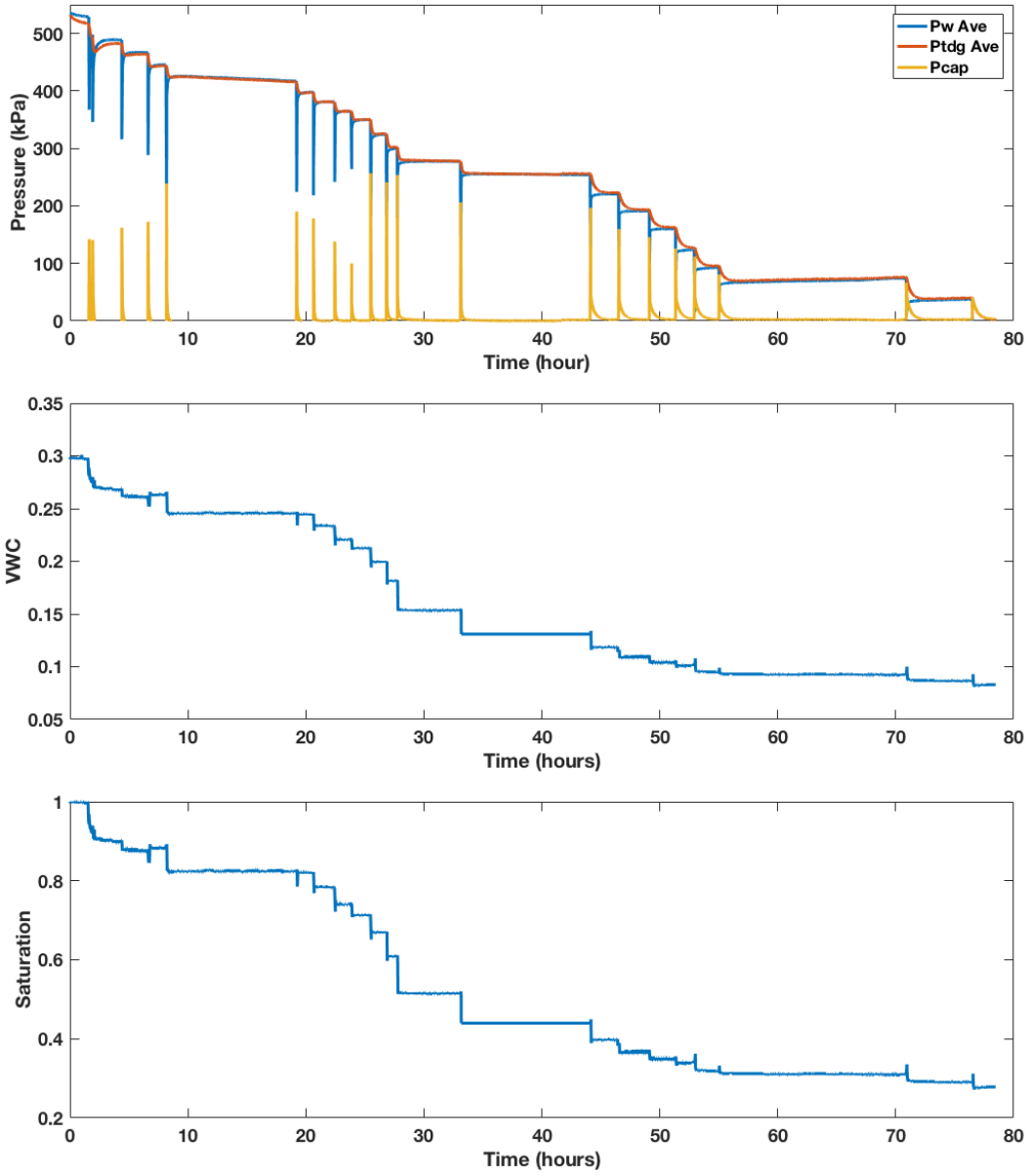

Figure A1.4: Data from experiment using 500 μm glass beads. Top figure shows P_W (blue), P_{TDG} (red), and P_{CAP} (orange). Middle figure shows Volumetric water content (VWC), and bottom figure is saturation when VWC data are divided by VWC value with maximum water saturation.

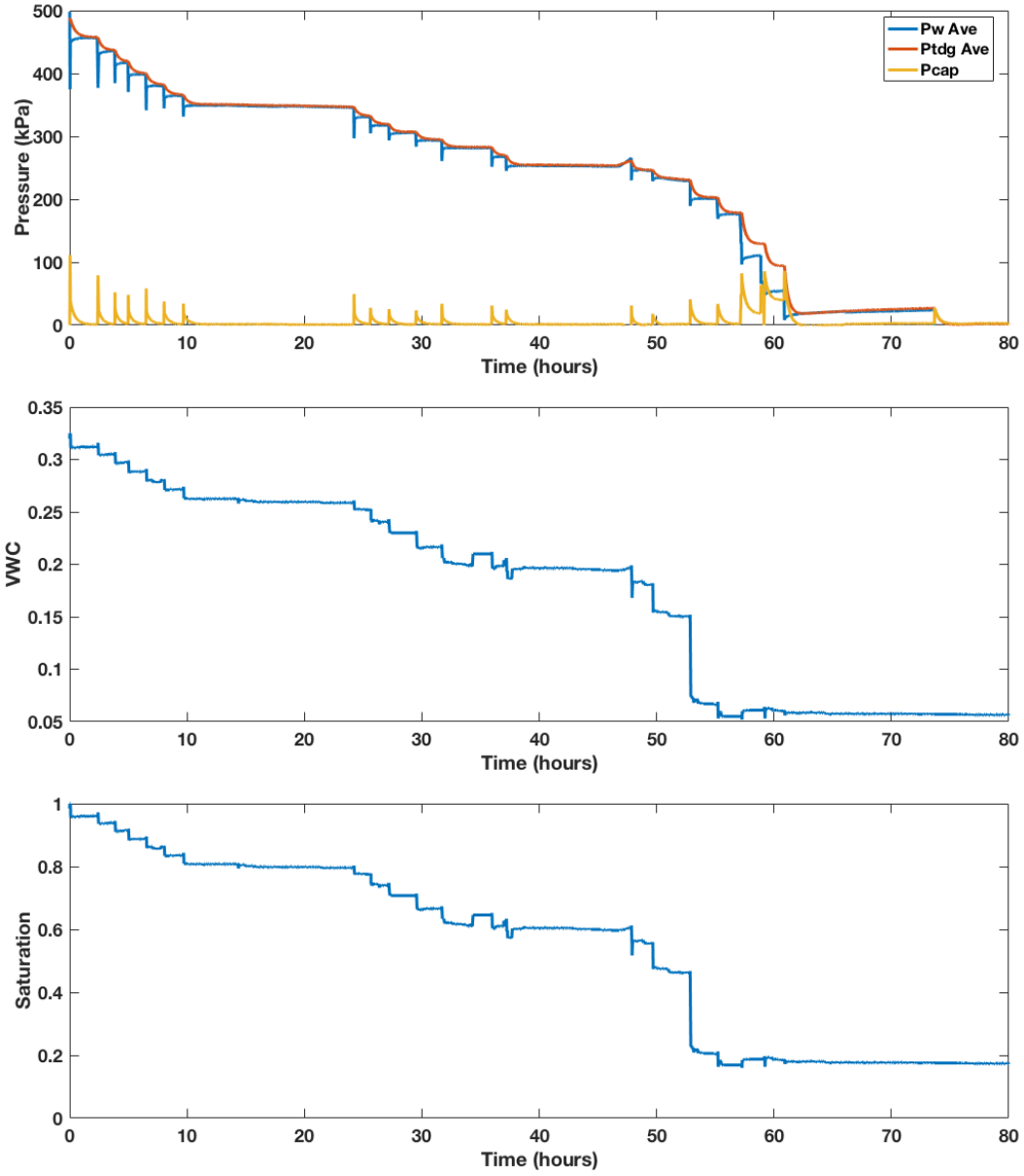

Figure A1.5: Data from experiment using 2000 μm glass beads. Top figure shows P_W (blue), P_{TDG} (red), and P_{CAP} (orange). Middle figure shows Volumetric water content (VWC), and bottom figure is saturation when VWC data are divided by VWC value with maximum water saturation.

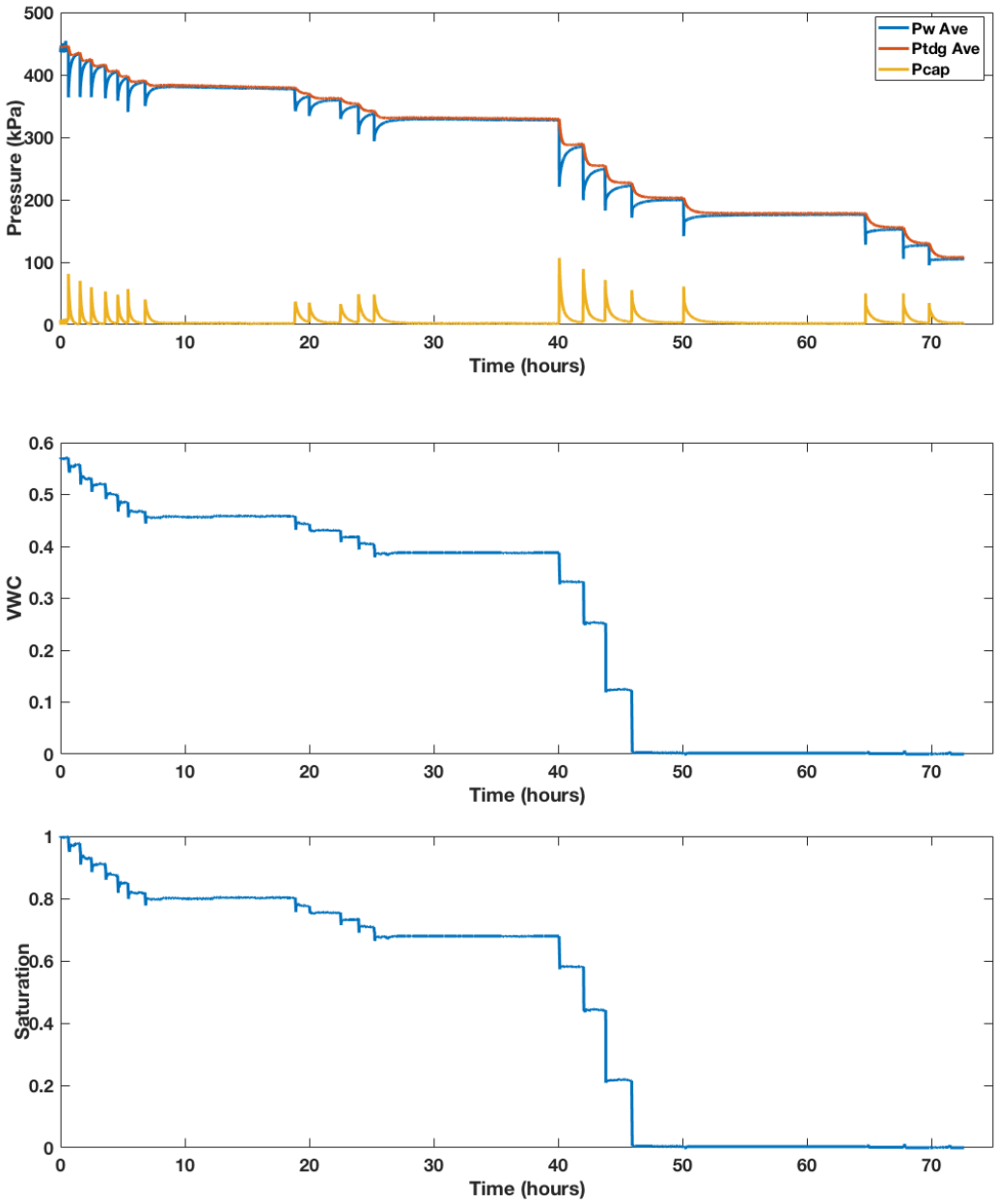

Figure A1.6: Data from control experiment (i.e., no glass beads). Top figure shows P_W (blue), P_{TDG} (red), and P_{CAP} (orange). Middle figure shows Volumetric water content (VWC), and bottom figure is saturation when VWC data are divided by VWC value with maximum water saturation.

APPENDIX A2: PHOTOGRAPHS FROM LABORATORY EXPERIMENTS

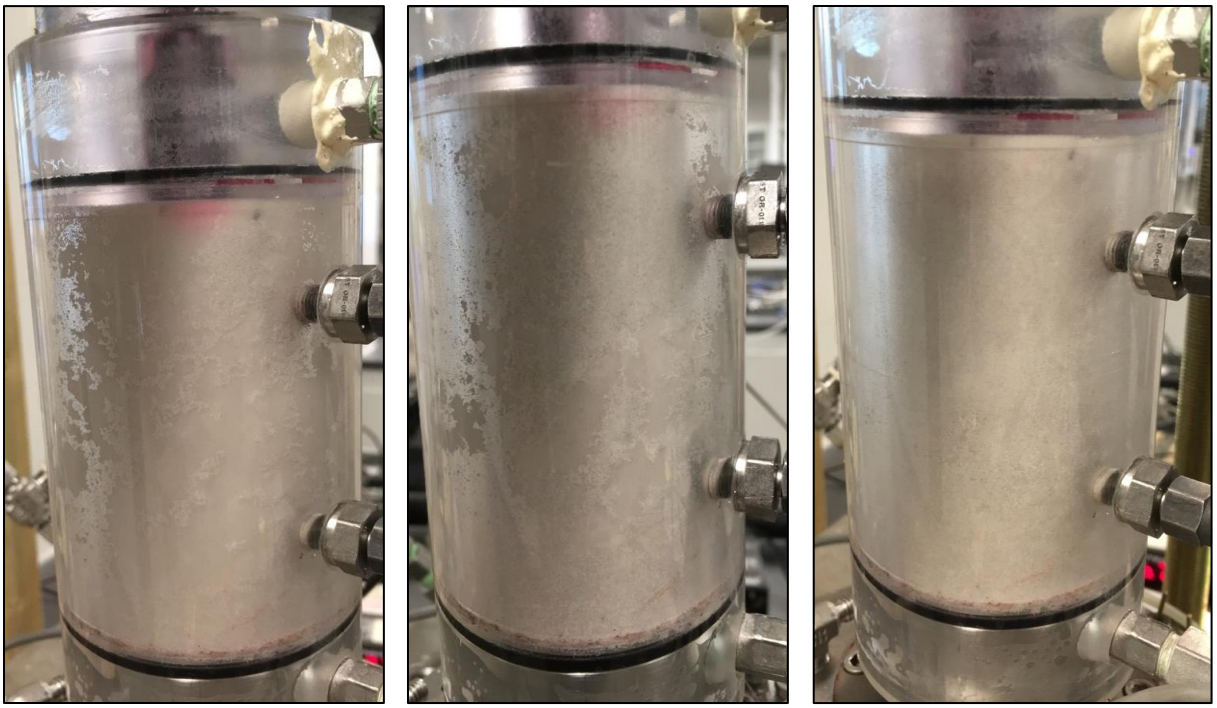

Figure A2.1: Photographs of loading cell containing 65 μm glass beads. Photographs taken after first, second, and fifth unloading events from left to right.

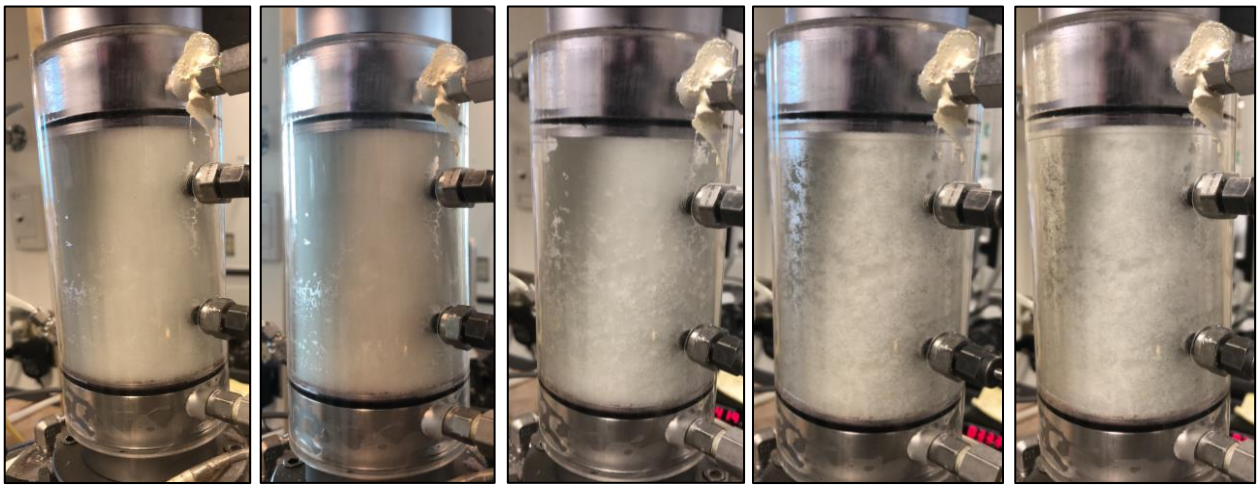

Figure A2.2: Photographs of loading cell containing 150 μm glass beads. Photographs taken before first, after first, seventh, sixteenth, and twenty-second unloading events from left to right.

Figure A2.3: Photographs of loading cell containing 300 μm glass beads. Photographs taken before first, after second, fifth, ninth, and twelfth unloading events from left to right.

Figure A2.4: Photographs of loading cell containing 500 μm glass beads. Photographs taken before first, after first, fourth, and seventh unloading events from left to right.

Figure A2.5: Photographs of loading cell containing 2000 μm glass beads. Photographs taken first, second, seventh, and thirteenth unloading events from left to right.

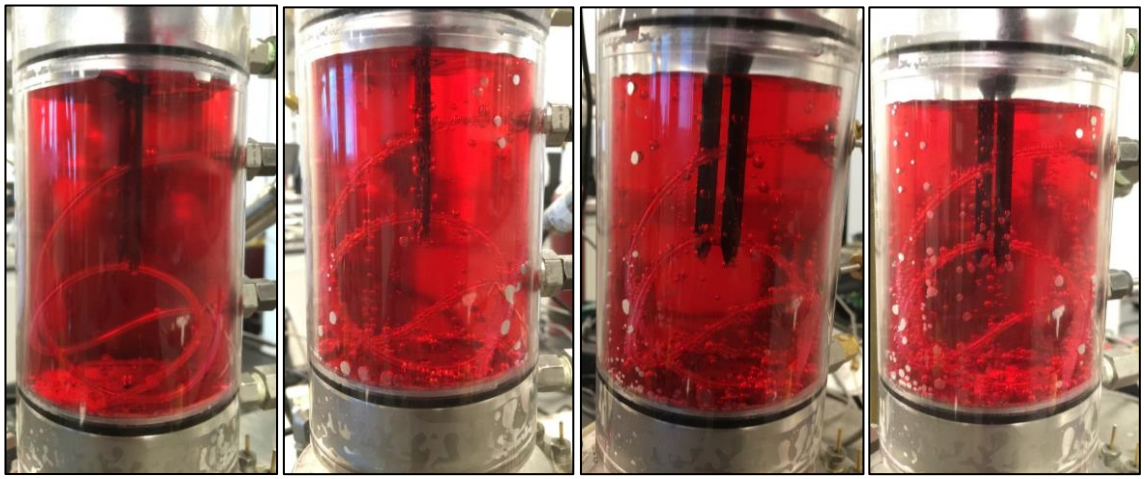

Figure A2.6: Photographs of loading cell containing no glass beads (i.e., control experiment). Photographs taken before first, after first, second, and third unloading events from left to right.

APPENDIX A3: EXPERIMENTAL ANALYSES

A3.1: Data calculations

1) Normalized pressure ($P_{W\,NORM}$), or fraction of initial P_W (kPa/kPa)

$$P_{W\,NORM} = \frac{P_W}{P_{W\,IN}}$$

2) Number of moles of CO_2 in the loading cell

Knowing initial VWC and total volume of the loading cell (V_{LC}), the total volume of water ($V_{W\,TOT}$) at the beginning of the experiment was calculated:

$$V_{W\,TOT} = V_{LC} \cdot VWC_i$$

Then, number of moles of $CO_{2(aq)}$ were calculated using Henry's Law:

$$[CO_{2(aq)}] = P_W \cdot k_H$$

$$n_{CO2(aq)} = [CO_{2(aq)}] \cdot V_{W\,TOT}$$

3) Number of moles of $CO_{2(g)}$ in the syringe after each unloading event (where SW is syringe water):

$$n_{CO2\ SW} = P_{ATM} \cdot k_H \cdot V_{SW}$$

4) Number of gaseous moles of $CO_{2(aq)}$ in the syringe after each unloading event (where SW is syringe gas):

$$n_{CO2\ SG} = \frac{P_{ATM} \cdot V_{SG}}{R \cdot T}$$

A3.2: Sample analyses from experimental data

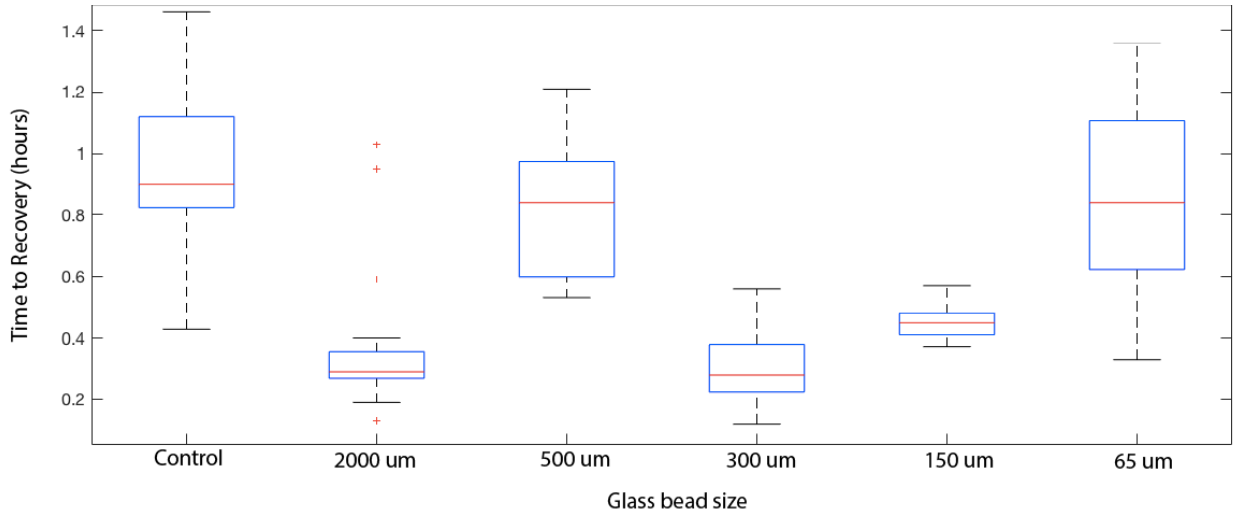

Figure A3.1: 'Box and whisker' plot showing the time to recovery (i.e., reaching equilibration) after each unloading event for each experiment. Central lines indicate the median values, the bottom and top of the box indicate the 25th and 75th percentiles, respectively, the whiskers indicate extreme data points, then then outliers are shown with + symbols

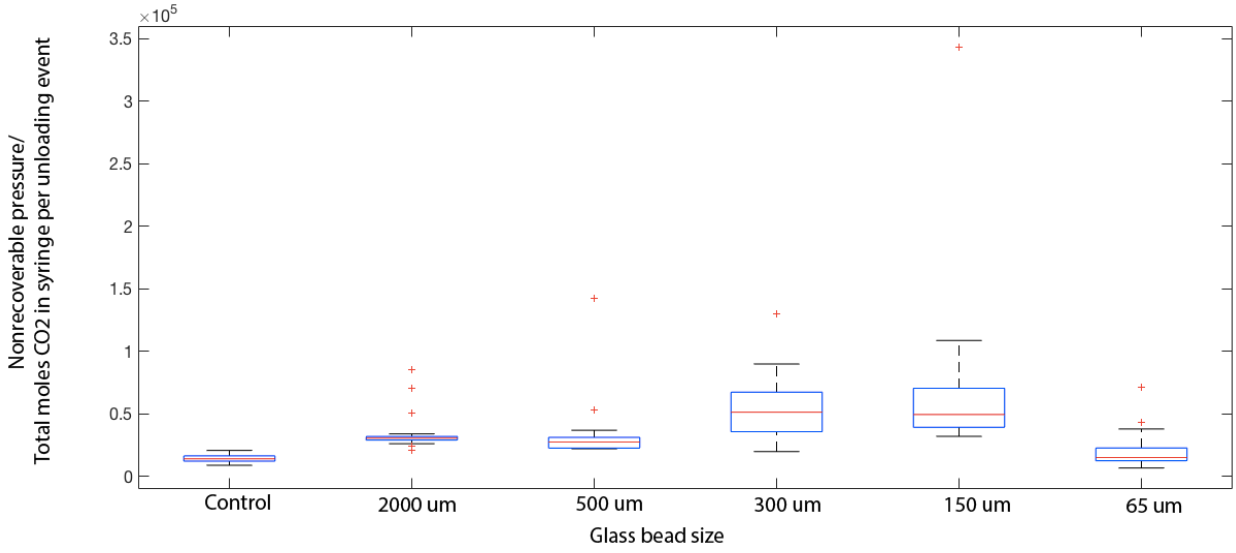

Figure A3.2: 'Box and whisker' plot showing the non-recoverable pressure (PNR) divided by the total number of moles removed from unloading after each unloading event. Central lines indicate the median values, the bottom and top of the box indicate the 25th and 75th percentiles, respectively, the whiskers indicate extreme data points, then then outliers are shown with + symbols

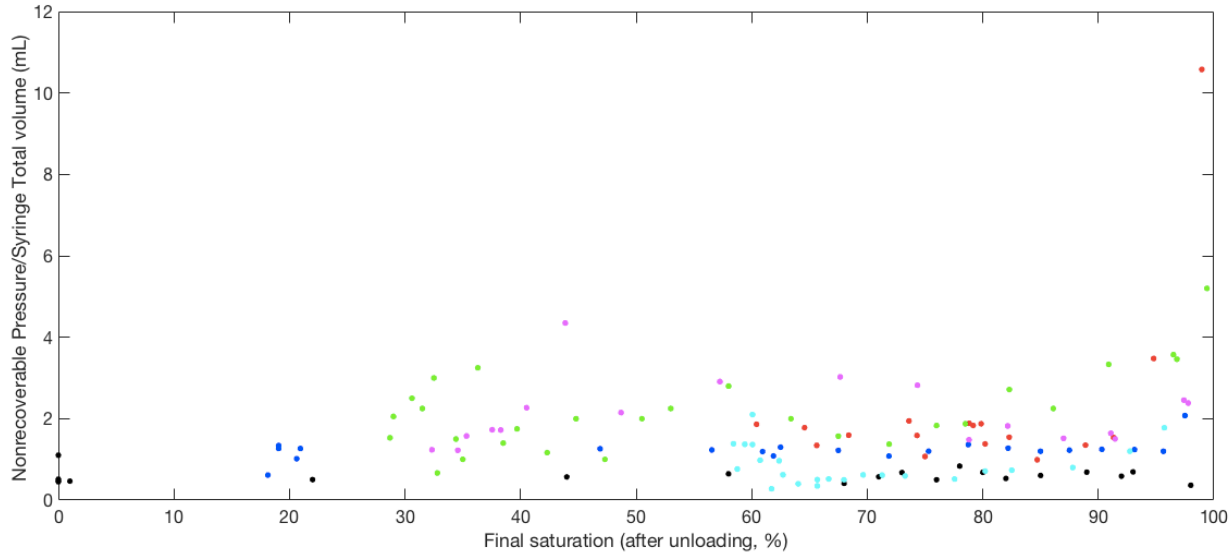

Figure A3.3: Experimental data of the unloading experiments (one experiment for each of the glass bead samples), comparing nonrecoverable pressure divided by the amount of water in the syringe after unloading, against saturation (%) after unloading.

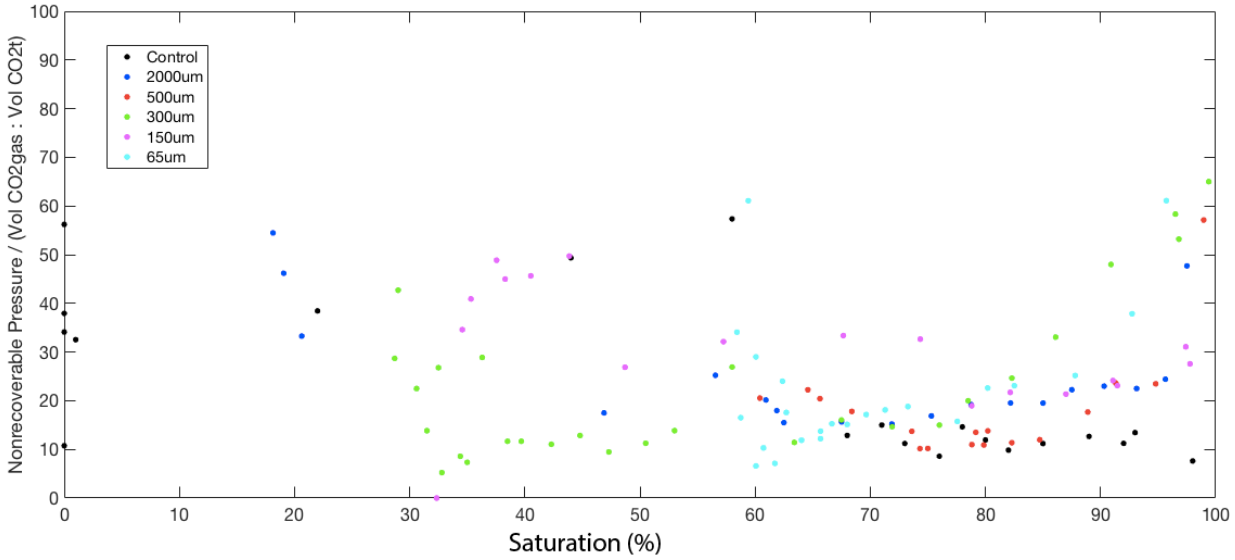

Figure A3.4: Experimental data of the unloading experiments (one experiment for each of the glass bead samples), comparing nonrecoverable pressure divided by the ratio of gas volume to total volume in the syringe (i.e., gas an water) from each unloading event, to against saturation (%) after unloading.

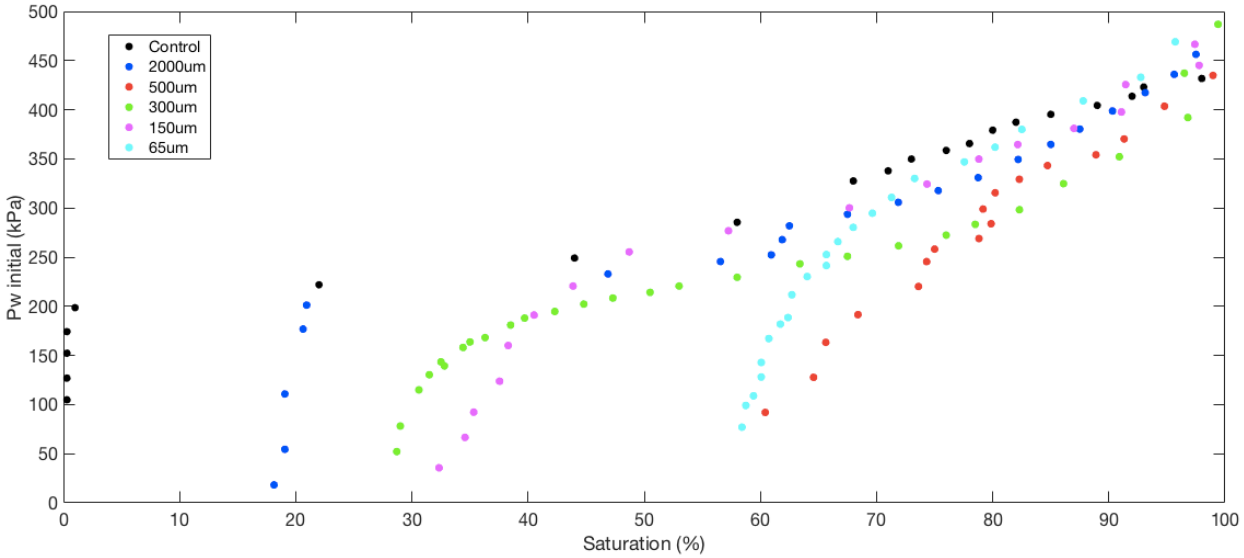

Figure A3.5: Experimental data of the unloading experiments (one experiment for each of the glass bead samples), comparing initial porewater pressure (P_W) to saturation (%).

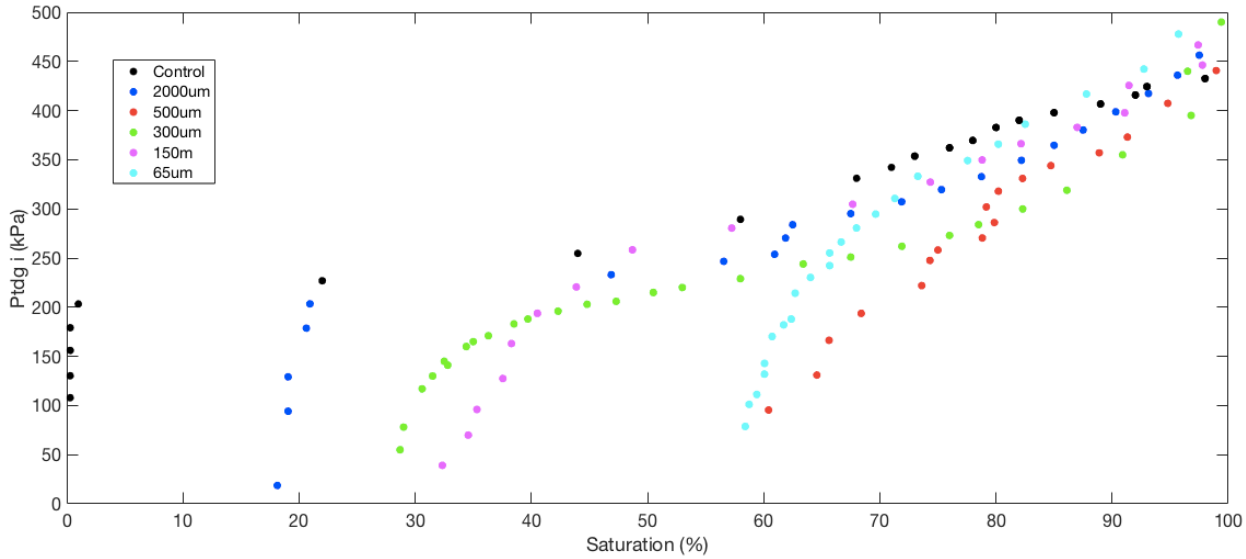

Figure A3.6: Figure A3.5: Experimental data of the unloading experiments (one experiment for each of the glass bead samples), comparing initial total dissolved gas pressure (P_{TDG}) to saturation (%).

APPENDIX A4: FREE PHASE GAS MODELLING

4.1 Model Scenario 1

Table A4.1: Quantitative assumptions and values used in Modelling Scenario 1.

Assumption Number	Variable	Value	Unit
1	Temperature, T	298	K
2	Porewater pressure, P_W	1	bar
3	Volume of water, V_W	0.015	L
4	Rate of gas production, dn/dt	$1.14x10^{-4}$ *	mol/L*day
5	Volume of free phase gas, V_{FPG}	Can vary	L
6	Interfacial tension, γ	$7.2x10^{-7}$	m*bar
7	Total volume of specimen, V_{TOT}	0.045	L
8	Porosity, n	0.33	unitless
9	Henry's Law coefficient, k_H	0.034	mol/kg*bar
10	Ideal Gas constant, R	$8.314x10^{-2}$	L*bar/K*mol

*$1.14x10^{-4}$ mol/L*day is 0.005g/L*day

Table A4.2: Qualitative assumptions and values used in Modelling Scenario 1.

Assumption Number	Assumption
10	Single gas species
11	Single, round FPG
12	Equilibrium partitioning between water and gas phases
13	Pw is constant, therefore 'drained system'
14	Constant rate of gas production
15*	Compressibility of **gas**, **water**, and **matrix** is negligible

* in the second model (below), water compressibility is incorporated

Table A4.3: Modelled values for Model Scenario 1 where compressibility of gas, water, and matrix were assumed to be negligible. In this model values were calculated based on the amount of gas that was produced for a given amount of time.

Time	Total number of moles, n_{TOT}	Aqueous gas concentration, Caq	Total dissolved gas pressure, P_{TDG}	Porewater pressure, P_W	Aqueous moles of gas, n_{AQ}	FPG moles, n_{FPG}	Volume of FPG, V	FPG radius, r	Capillary pressure, P_{CAP}	Buoyancy pressure, P_{BOUY}
Day	mol	mol/L	bar	bar	mol	mol	L	m	bar	bar
1	0.0001	0.01	0.23	1.00	1.14E-04	N/A	N/A	N/A	N/A	N/A
5	0.0006	0.04	1.00	1.00	5.05E-04	6.33E-05	0.0016	1.25E-07	11.54163	2.45E-06
10	0.0011	0.08	1.00	1.00	5.05E-04	6.31E-04	0.0156	1.24E-06	1.15664	2.44E-05
15	0.0017	0.11	1.00	1.00	5.05E-04	1.20E-03	0.0297	2.37E-06	0.60883	4.64E-05
50	0.0057	0.38	1.00	1.00	5.05E-04	5.18E-03	0.1283	1.02E-05	0.14108	2.00E-04
100	0.0114	0.77	1.00	1.00	5.05E-04	1.09E-02	0.2690	2.14E-05	0.06726	4.20E-04

Calculations

1. Total number of moles of gas was calculated using:

$$n_{TOT} = time * dn/dt$$

2. Concentration of gas in dissolved phase calculated by:

$$C_{aq} = \frac{n_{TOT}}{V_W}$$

3. Estimate P_{TDG} with Henry's Law, such that:

$$P_{TDG} = \frac{C_{aq}}{k_H}$$

4. Determine whether continued gas produced will end up in dissolved phase or gaseous phase. When P_{TDG} is equal to or greater than P_W, then any gas produced will go into the free gas phase (this is known as ebullition or bubbling point, P_{BUB}).

5. Past the point of gas saturation n_{FPG} can be determined by:

$$n_{FPG} = n_{TOT} - n_{aq\ Max}$$

   where $n_{aq\ Max}$ is determined by Henry's Law at the P_W.

6. Using the Ideal Gas Law, calculate volume of FPG such that:

$$V = \frac{nRT}{P}$$

7. Calculate radius of FPG using volume:

$$r = \sqrt[3]{\frac{3V}{4\pi}}$$

8. Knowing radius, capillary pressure, P_{CAP}, was calculated:

$$P_{CAP} = \frac{2\gamma * cos\theta}{r}$$

9. Finally, buoyancy pressure, P_{Buoy} was calculated knowing the FPG size:

$$P_{BUOY} = (\sigma_W - \sigma_{FPG}) * g * h_{FPG}$$

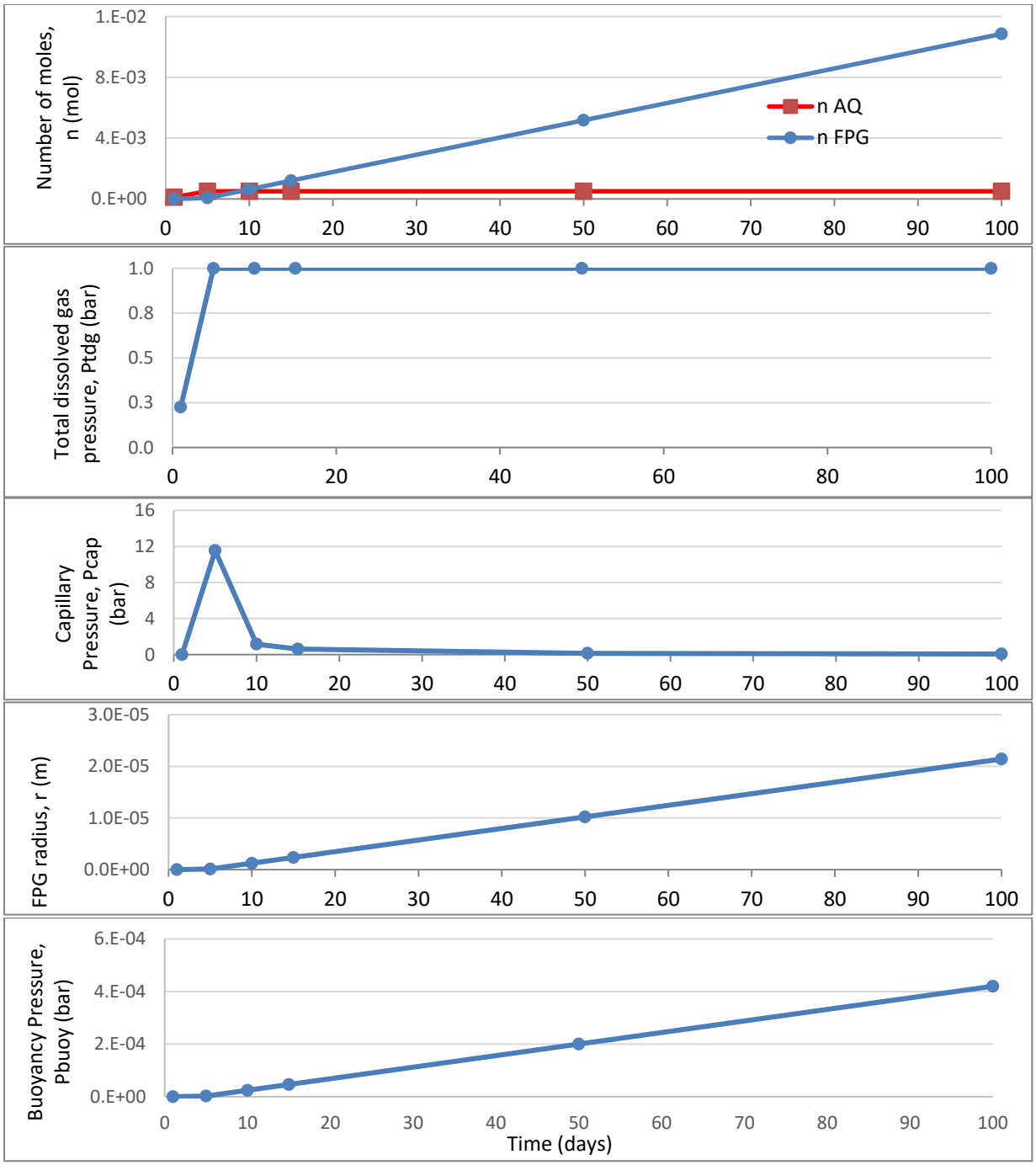

Figure A4.1: Model results for Scenario 1. Graphs show quantitative results for a) number of moles of FPG and dissolved gas, b) P_{TDG}, c) P_{CAP}, d) FPG body radius, assuming spherical bubble, and e) buoyancy pressure of the FPG body.

Model Scenario 2

Table A4.4: Quantitative assumptions and values used in Modelling Scenario 2.

Assumption Number	Variable	Value	Unit
1	Temperature, T	298	K
2	Volume of water, V_W	0.015	L
3	Rate of gas production, dn/dt	$1.14x10^{-4}$ *	mol/L*day
4	Volume of free phase gas, V_{FPG}	Can vary	L
5	Interfacial tension, γ	$7.2x10^{-7}$	m*bar
6	Total volume of specimen, V_{TOT}	0.045	L
7	Porosity, n	0.33	unitless
8	Henry's Law coefficient, k_H	0.034	mol/kg*bar
9	Ideal Gas constant, R	$8.314x10^{-2}$	L*bar/K*mol
10	Compressibility of matrix, α	$1.0x10^{-7}$ **	$m*s^2/kg$

*$1.14x10^{-4}$ mol/L*day is 0.005g/L*day
** compressibility for a typical sandstone

Table A4.5: Qualitative assumptions and values used in Modelling Scenario 2

Assumption Number	Assumption
10	Single gas species
11	Single FPG
12	Equilibrium partitioning between water and gas phases
13	Constant rate of gas production
14	Compressibility of **gas** and **matrix** is negligible

Table A4.6: Modelled values for Model Scenario 1 where compressibility of gas and matrix were assumed to be negligible. In this model values were calculated based on the amount of gas that was produced for FPG body of assigned radius. It should be notes that time is indicative of the time required to produce the moles of gas after P_{TDG} reaches bubbling point, P_{BUB}.

FPG radius, r	FPG volume, V	Capillary pressure P_{CAP}	Change in effective stress, $\Delta\sigma_{eff}$	Change in porewater pressure, ΔP_W	Initial Porewater pressure, $P_{W\,i}$	Final Porewater pressure, $P_{W\,f}$	Aqueous moles,	FPG moles, n_{FPG}	Total moles of gas, n_{TOT}	Time	Total Dissolved Gas Pressure, P_{TDG}	Buoyancy Pressure, P_{BUOY}
m	m^3	bar	bar	bar	bar	bar	n_{AQ}	mol	mol	days	bar	bar
0	0	NA	0	0	1	1.00	0.0005	0	0.00049	4.3120	1	0.0E+00
1.25E-07	8.1E-21	11.54	-5.5E-12	5.5E-12	1.00	1.00	0.0005	3.3E-19	5.0E-04	4.4431	1.00	2.4E-06
1.24E-06	8.1E-18	1.16	-5.4E-09	5.4E-09	1.00	1.00	0.0005	3.3E-16	5.0E-04	4.4431	1.00	2.4E-05
2.37E-06	5.5E-17	0.61	-3.2E-08	3.2E-08	1.00	1.00	0.0005	2.2E-15	5.0E-04	4.4431	1.00	4.6E-05
1.02E-05	4.5E-15	0.14	-3.0E-06	3.0E-06	1.00	1.00	0.0005	1.8E-13	5.0E-04	4.4431	1.00	2.0E-04
2.14E-05	4.1E-14	0.07	-2.5E-05	2.5E-05	1.00	1.00	0.0005	1.7E-12	5.0E-04	4.4431	1.00	4.2E-04

Calculations

1. Unlike the first model, it is assumed here that the water is already gas saturation (i.e., P_{BUB} has already been exceeded), and FPGs have formed

2. Assuming a FPG radius, volume of FPG was calculated:
$$V = \frac{4}{3}\pi * r^3$$

3. Knowing radius, capillary pressure, P_{CAP}, was calculated:
$$P_{CAP} = \frac{2\gamma * cos\theta}{r}$$

4. From the FPG volume, change in effective stress can be calculated:
$$\Delta\sigma_{eff} = \frac{\Delta V_T / V_T}{\alpha}$$

5. Knowing the change in effective stress from the FPG, change in porewater pressure can be found using:
$$\Delta\sigma_T = \sigma_{eff} + P_W$$

   In this model, there is no assumed change in total stress. As such, any change in effective stress is equal and opposite in magnitude to the change in porewater pressure.
$$\Delta\sigma_T = 0$$
$$\Delta\sigma_{eff} = -\Delta P_W$$

6. New porewater pressure resulting from the FPG can be calculated using:
$$P_{W\,f} = P_{W\,i} + \Delta P_W$$

7. Calculate n_{AQ} using Henry's Law:
$$n_{AQ} = k_H * V_W * P_W$$

8. Calculate n_{FPG} using the Ideal Gas Law:
$$n_{FPG} = \frac{PV}{RT}$$

9. Add previous two to get n_{TOT}:
$$n_{TOT} = n_{AQ} + n_{FPG}$$

10. Knowing rate of gas production, find time to produce n_{TOT}:

$$time = \frac{n_{TOT}}{dn/dt}$$

11. Also calculate P_{Buoy}

$$P_{BUOY} = (\sigma_W - \sigma_{FPG}) * g * h_{FPG}$$

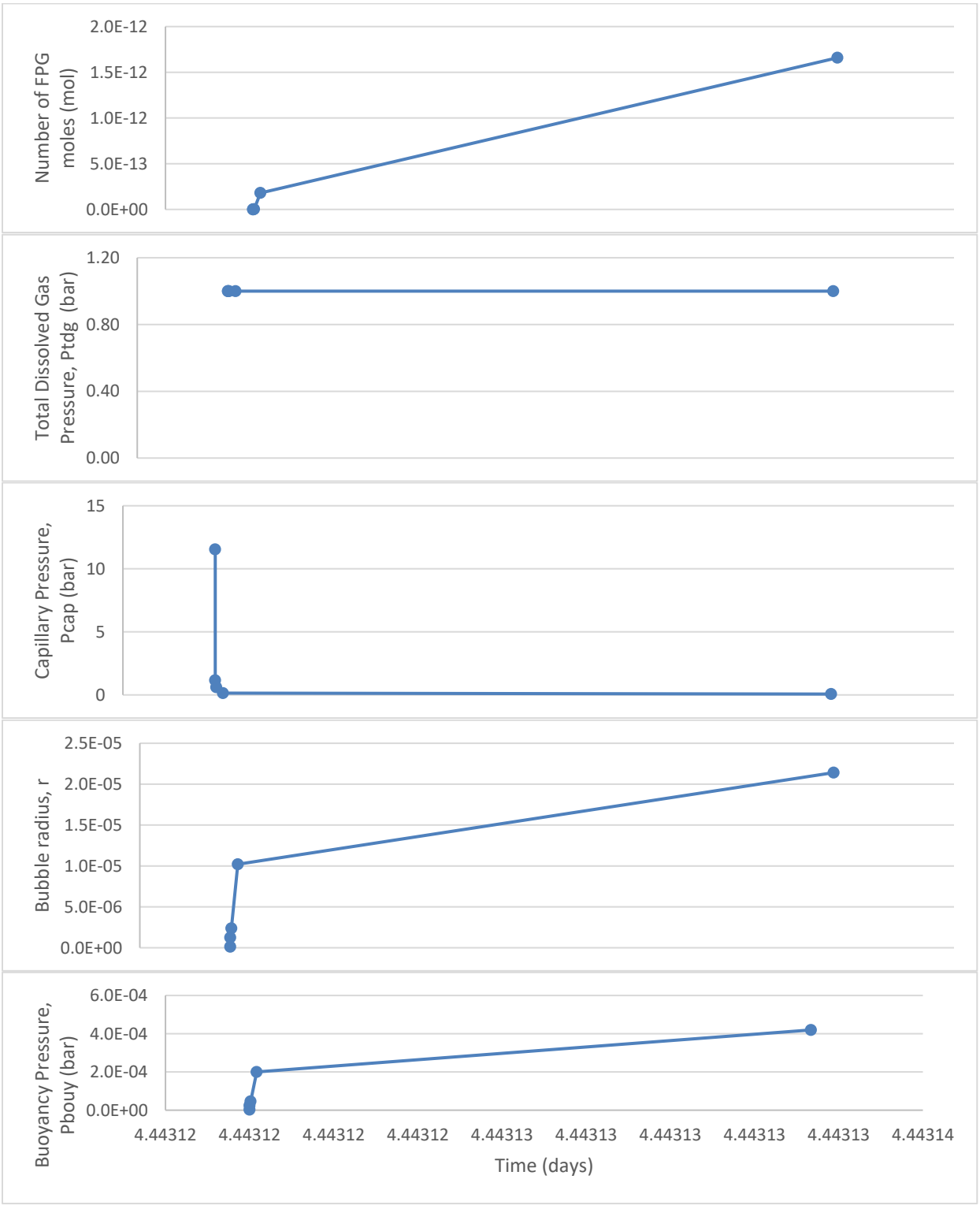

Figure A4.1: Figure A4.1: Model results for Scenario 2. Graphs show quantitative results for a) number of moles of FPG and dissolved gas, b) P_{TDG}, c) P_{CAP}, d) FPG body radius, assuming spherical bubble, and e) buoyancy pressure of the FPG body.